In Press

Moist Static Energy Budget of MJO-like disturbances in the atmosphere of a zonally symmetric aquaplanet

Joseph Allan Andersen[1]

Department of Physics, Harvard University, Cambridge, Massachusetts

Zhiming Kuang

Department of Earth and Planetary Science and School of Engineering and Applied Sciences, Harvard University, Cambridge, Massachusetts

[1] *Corresponding author address*: Joseph Andersen, Department of Physics, Harvard University, Cambridge, MA 02138.
E-mail: jaanders@fas.harvard.edu

Abstract

A Madden-Julian Oscillation (MJO)-like spectral feature is observed in the time-space spectra of precipitation and column integrated Moist Static Energy (MSE) for a zonally symmetric aquaplanet simulated with Super-Parameterized Community Atmospheric Model (SP-CAM). This disturbance possesses the basic structural and propagation features of the observed MJO.

To explore the processes involved in propagation and maintenance of this disturbance, we analyze the MSE budget of the disturbance. We observe that the disturbances propagate both eastwards and polewards. The column integrated long-wave heating is the only significant source of column integrated MSE acting to maintain the MJO-like anomaly balanced against the combination of column integrated horizontal and vertical advection of MSE and Latent Heat Flux. Eastward propagation of the MJO-like disturbance is associated with MSE generated by both column integrated horizontal and vertical advection of MSE, with the column long-wave heating generating MSE that retards the propagation.

The contribution to the eastward propagation by the column integrated horizontal advection of MSE is dominated by synoptic eddies. Further decomposition indicates that the advection contribution to the eastward propagation is dominated by meridional advection of MSE by anomalous synoptic eddies caused by the suppression of eddy activity ahead of the MJO convection. This suppression is linked to the barotropic conversion mechanism; with the gradients of the low frequency wind experienced by the synoptic eddies within the MJO envelope acting to modulate the Eddy Kinetic Energy.

The meridional eddy advection's contribution to poleward propagation is dominated by the mean state's (meridionally varying) eddy activity acting on the anomalous MSE gradients associated with the MJO.

1. Introduction

In observations of satellite records of equatorial Outgoing Longwave Radiation (OLR, e.g. Liebmann and Smith 1996), there are patterns of enhanced convection and precipitation organized on planetary scales. The strongest and largest of these convective structures propagate eastwards at about 5 m/s with periods in the range of 30 to 90 days from the Indian Ocean to the central Pacific, coupled to planetary scale wind, temperature, and moisture anomalies. This disturbance is known as the Madden-Julian Oscillation (MJO), originally identified in tropical zonal wind soundings by Madden and Julian (1971, 1972). The MJO dynamics involve planetary scale circulations interacting with mesoscale convective systems and potentially the ocean, making it a challenging phenomenon to understand (e.g. Zhang 2005).

Understanding the MJO phenomena is important to our grasp of the tropical atmosphere and climate for many reasons. MJO related variations dominate the intraseasonal variability of the tropical ocean-atmosphere system, linking the variabilities of climate and weather (e.g. Lau and Wu 2010). For example, the MJO is seen to influence the rainfall over virtually all regions of the tropics and the subtropics: the Asian Monsoon (e.g. Lau and Chan 1986, Sui and Lau 1992, Lawrence and Webster 2002); the Australian Monsoon (e.g. Hendon and Liebmann 1990); over the Indonesian archipelagos (Hidayat and Kizu 2010); along the west coast of North America (Mo and Higgins 1998, Jones 2000, Bond and Vecchi 2003); in South America (Paegle *et al.* 2000, Liebmann et al 2004); and in Africa (Matthews 2004).

The MJO has also been observed to modulate the genesis of tropical cyclones in the

Pacific and Caribbean basins (e.g. Liebmann *et al.* 1994, Nieto Ferrira *et al.* 1996, Maloney and Hartmann 2000, Hall *et al,* 2001, Higgins and Shi 2001, Frank and Roundy 2006). It has been observed that improved forecasts of MJO dynamics may help improve short term Tropical Cyclone forecasting (e.g. Leroy and Wheeler 2008). The MJO affects the global medium and long range weather forecasts (e.g. Ferranti *et al.* 1990, Hendon *et al.* 2000, Jones and Schemm 2000); modulates the global angular momentum and the length of the day (e.g. Langley *et al.* 1981, Gutzler and Ponte 1990, Weickmann *et al.* 1997); and modulates the Earth's electric and magnetic fields, with influence upon lightning activity (e.g. Anyamba *et al.* 2000).

MJO events are usually observed in the Indian and Western Pacific Oceans as large-scale, eastward propagating regions of strong, deep convection and precipitation separating regions of weak convection. The structure usually has a zonal wavenumber of 1 or 2, with a single active region existing at a time. An overturning zonal circulation that extends vertically through the entire troposphere connects the active and inactive phases. The circulation creates zonally converging winds in the boundary layer and lower troposphere (up to about 850 hPa) and zonally diverging winds at about 200 hPa (e.g. Madden and Julian 1972 and Zhang 2005). The coupled wind-convection system propagates at around 5 m/s. The MJO events can be clearly seen in Hovmöller plots of many observed quantities, such as equatorial zonal wind (e.g., Xie and Arkin 1997), or as a very strong peak in wavenumber-frequency spectra of tropical variables such as OLR (e.g. Wheeler and Kiladis 1999).

The description of the MJO as a purely eastward moving monolith of convection is not the whole picture. For example, the MJO convective region is a multiscale structure, consisting of an ensemble of convective systems moving at many different speeds in all directions (e.g. Nakazawa 1988). The convection in these mesoscale and smaller systems is enhanced by the large-scale conditions in the MJO active region and the motion of the active region is reflected in a general eastward trend in the locations these systems develop and then decay. Another important fact to consider is that the MJO propagation is not always strictly eastwards - meridional motion, generally into the summer hemisphere, is observed over the east Pacific and over southern Asia in some seasons (Typically Boreal Summer; Wang and Rui 1990a).

The MJO is one of the dominant structures in the tropical atmosphere and has been observed for almost four decades, so its structure has been quite well determined (e.g. Hendon and Salby 1994, Lau and Sui 1997, Yanai *et al.* 2000, Kikuchi and Takayabu 2004, Kiladis *et al.* 2005, Haertel *et al.* 2008), although a sufficiently accurate energy budget remains elusive. At the same time, the theoretical understanding of the mechanisms responsible for its growth and propagation has not kept pace (e.g., Zhang 2005, Waliser *et al.* 2006). Because the convectively coupled Kelvin Waves (KW) have many basic features in common with the MJO (propagation direction, scale, wind field structure), and because theories of the equatorial waves have shown some successes (e.g. Matsuno 1966, Wang 1988, Majda and Shefter 2001, Andersen and Kuang 2008, Kiladis *et al.* 2009), the KW and the other equatorially trapped shallow water waves are commonly used as a fundamental part of MJO theories. [2]

---

[2] The equatorially trapped shallow water waves arise from an analysis of the anomalies in temperature and wind of zonally symmetric atmosphere linearized about a stationary

However, the KW propagates much faster than the MJO and is quite distinct from the MJO in spectral space. This leads to the question - in what ways does the convectively coupled KW differ from the MJO? For either of these wave types to exist in observations, some process or processes must supply energy (or an analogous quantity) to overcome dissipation selectively at the timescales, wavelengths and velocities of the disturbances. Most theories of the KW assume that the source of the energy for the wave comes from an interaction between convective heating and the large-scale temperature structure of the wave, with scale selection due to the varying sign of the heating/warm anomaly overlap. Such theories have had success replicating the nature of the KW (and other “rotating shallow water” modes) in simple models (e.g. Mapes 2000, Khouider and Majda 2006, Kuang 2008, Andersen and Kuang 2008). Any theory of the MJO requires column Moist Static Energy (MSE) variance to be generated at intraseasonal and planetary scales, with slow eastward propagation. There are a number of potential sources of column MSE variability that are often considered:

---

mean state. Under the assumptions of constant stratification and a rigid upper boundary on the troposphere, the vertical structure equations can be separated from the horizontal dynamics, which are identical to the equations for shallow water modes, with the separation constant identified as the equivalent depth. Due to the rotation of the earth, the shallow water system has a number of specific modes propagating along the equator, as determined by Matsuno (1969). The convectively coupled shallow water waves tend to exist and propagate because of the interactions between convective heating and the temperature anomalies of the waves.

1) An independently existing forcing such as a standing oscillation in the convection over the warm pool, with MJO propagation as a passive atmospheric response (e.g. Zhang and Hendon 1997);

2) The column MSE variability is generated by the coupling of convection and circulation. An example of this sort of mechanism is Wave-CISK (e.g. Lau and Peng 1987), where convection releases latent heat that drives further convection by creating more low-level convergence;

3) Wind Induced Surface Heat Exchange (WISHE; Emanuel 1987, Neelin *et al.* 1987), where surface wind anomalies lead to surface flux anomalies that may provide an energy source to the convection;

4) Instability arising from frictional moisture convergence feedback (e.g. Wang 1988);

5) Thermodynamic feedbacks - such as water vapor accumulation (Blade and Hartmann 1993) and convection-radiation feedback (Hu and Randall 1994, 1995, Raymond 2001).

It is in this last paradigm that we will be interpreting our observations, so it bears further exposition. The Recharge-Discharge mechanism, an extension of the thermodynamic feedback idea, is based upon the build up of MSE in the columns over the tropical ocean that occurs before the MJO deep convection. This convection and the succeeding processes discharge the column MSE anomaly, which is then recharged by the large-scale processes (e.g. Hendon and Liebmann 1990, Blade and Hartmann 1993, Hu and Randall 1994, Maloney and Hartmann 1998, Kemball-Cook and Weare 2001, Myers and Waliser 2003, Sobel and Gildor 2003, Kiladis *et al.* 2005, Agudelo *et al. 20*06, Tian *et al.* 2006, Benedict and Randall 2007, Maloney 2009). In order for Recharge-Discharge to constitute an instability mechanism, there must be sources of column MSE collocated in space and time with positive column MSE anomalies (similarly for sinks and negative MSE anomalies).

Recent studies appear to indicate that the moistening of the free troposphere (leading to a build up of MSE) is needed before the onset of strong deep convection (e.g. Brown and Zhang 1997, Sherwood 1999, Raymond 2000, Redelsperger *et al.* 2002, Ridout 2002, Bretherton *et al.* 2004, Derbyshire *et al.* 2004, Sobel *et al.* 2004, Takemi *et al.* 2004, Roca *et al.* 2005, Kuang and Bretherton 2006, Peters and Neelin 2006). Similarly, parameterizations that demonstrate a strong sensitivity to free-troposphere humidity have been shown to increase intraseasonal variability in GCMs (e.g. Wang and Schlesinger 1999, Woolnough *et al. 20*01). Ocean heat content may also be built up before the onset of convection, with the surplus heat flowing into the atmosphere during the convective phase (e.g. Sobel and Gildor 2003, Stephens *et al.* 2004, Agudelo *et al.* 2006). In general, the MSE budget during MJO events is not well understood, although there have been recent numerical studies of this question (Maloney 2009, Maloney *et al.* 2010).

In another recent study of the MSE budget of large-scale tropical flows (Kuang 2011), it has been shown that the large-scale flow induced by MSE anomalies in a column, while acting to dissipate the column MSE anomaly, will become less efficient at doing so with longer wavelengths. This is because the temperature anomalies required to generate the large-scale flow increases with wavelength, affecting the vertical distribution of convection. This is suggested as a possible scale selection mechanism explaining the limitation of the MSE driven waves to long wavelengths.

In analogy to the buoyancy driven KW theories, we will interpret the MJO growth and propagation as the overlap between “moist” air and “moistening”. In this context and throughout this paper, “moist” is synonymous with a positive MSE anomaly and “moistening” with an MSE source.

The basic picture of the MSE budget in the MJO established to date is as follows: The shallow convection and circulations ahead of the convective anomaly have a moistening tendency, contributing to the MSE build up before the deep convection (e.g. Johnson *et al.* 1999, Kikuchi and Takayuba 2004, Kiladis *et al.* 2005, Benedict and Randall 2007). Column-integrated MSE may then be discharged during strong convective and stratiform heating. The large-scale circulations in the Western Pacific and Indian Ocean are strongly determined by the deep convection and have been observed to export MSE for the convecting columns on average (e.g. Neelin and Held 1987, Back and Brethton 2006). In this region the MJO amplitude is strongest and the MSE discharge appears to be enhanced by the MJO deep convective and stratiform stages (e.g. Johnson *et al.* 1999, Kiladis *et al* 2005).

MSE discharge during MJO convection may be modified by cloud-radiation and wind-evaporation feedbacks, which could reduce or change the sign of the MSE tendency (e.g. Raymond 2001, Lin and Mapes 2004, Peters and Bretherton 2006, Sugiyama 2009a, 2009b). Intraseasonal wind speed and latent heat flux anomalies are observed to have a positive covariance with the intraseasonal precipitation (e.g. Zhang 1996, Raymond *et al.* 2003, Masunaga *et al.* 2006, Maloney and Esbensen 2007, Araligidad and Maloney 2008) and wind-evaporation feedbacks have been found to be important for supporting the intraseasonal convection in modeling studies (e.g. Raymond 2001, Maloney and Sobel 2004, Fuchs and Raymond 2005, Sugiyama 2009a, 2009b). However, the WISHE feedbacks are not generally in the original sense of WISHE, where easterly anomalies interact with mean state easterlies to create enhanced flux under the warm anomaly region in KW-type circulation, pulling convection forwards in space (e.g. Emanuel 1987, Neelin et al 1987, Emanuel *et al.* 1994) to create overlap between the convective heating and the warm anomaly. The intraseasonal latent heat flux-precipitation relationships are consistent with the more general role of enhanced wind speed in supporting tropical precipitation – particularly in regions of high column relative humidity (e.g. Back and Bretherton 2005). Observations also suggest that horizontal advection of temperature and moisture from the cooler, drier subtropics is an important regulatory mechanism for the atmospheric MSE budget and MJO deep convection (e.g. Mapes and Zuidema 1996, Myers and Waliser 2003, Back and Bretherton 2006).

Model analysis of the MSE budget in CAM3 with a realistic basic state shows that horizontal advection plays an important role in regulating the discharge-recharge cycle. The advection effect is dominated by the tropical synoptic scale eddies (Maloney 2009). Maloney (2009) observed a buildup of column MSE in advance of intraseasonal precipitation within low-level easterly anomalies and a discharge of MSE during and after the precipitation, within low-level westerlies. The recharge-discharge budget of the MSE is driven by horizontal advection (somewhat opposed by a mostly out of phase latent heat flux), which is itself dominated by the meridional advection of dry subtropical air into the MJO region by atmospheric eddies, which are suppressed by the anomalous large-scale winds ahead of the convection and enhanced behind.

While the eastward propagating MJO dominates the tropical intraseasonal variability, it is not the only significant source of variability on these timescales. For example, there are prominent northward propagating oscillations during the Asian monsoon (Yasunari 1979, Lau and Chan 1986, Wang and Rui 1990a). It has been observed that the MJO eastward propagation weakens during boreal summer (Madden 1986, Wang and Rui 1990a) and a northward propagating feature in the intraseasonal fequencies becomes prominent over the Indian summer monsoon region (e.g. Yasanuri 1979, Sikka and Gadgil 1980, Krishnamurti and Subrahmanyam 1982, Goswani 2005). Several theories have been suggested to explain this observation:

1) Northward propagation as a result of feedback between the hydrological cycle and the dynamics over India (Webster 1983). Land sensible heat flux in the boundary layer can destabilize the atmosphere ahead of the ascending zone, causing northward shifts in the convective region;

2) The interaction between equatorial moist KW and the monsoon flow can generate (in numerical experiments) unstable quasi-geostrophic baroclinic waves in the monsoon region, weakening the equatorial disturbance (Lau and Peng 1990);

3) In a model, continuous NW propagating Rossby waves are seen to emanate from an equatorial KW as it crosses the maritime continent, creating the northward moving rainbands (Wang and Xie 1997);

4) Examination of the poleward propagating rainbands in a high resolution cloud-system resolving model indicates that poleward propagation may be due to convectively coupled beta drift of low-level vorticity anomalies (Boos and Kuang 2010).

It seems likely that the poleward propagating modes originate from the same disturbance as the eastward propagating MJO (e.g. Lawrence and Webster 2002, Jiang *et al.* 2004). However, it is often observed that the poleward and eastward disturbances separate over the Indian Ocean and may propagate independently.

In this paper, we describe the observation and MSE budget analysis of an MJO-like disturbance in the Super-Parameterized CAM (SPCAM) on a zonally symmetric aquaplanet. This work differs from similar, previous analyses in several ways. Firstly, our analysis is of a model using a more explicit representation of convection - the super-parameterization (described below). This improves aspects of the realism of the simulation. Secondly, we use a zonally symmetric basic state, which simplifies the analysis and diagnosis of the energy budget. Thirdly, the MJO observed in our model shows both eastwards and polewards propagation - a phenomenon not reported in earlier works - which allows us to investigate another aspect of the intraseasonal dynamics (albeit in simplified form).

In section 2, the model and the experimental setup is described. Also, basics of the model output are analyzed: Time-space spectra are used to identify the MJO-like signals in the model, which are also visualized in Hovmöller diagrams of the tropics. Towards an understanding of the processes involved in this signal, we present a composite evaluation of the leading terms of the MSE budget of MJO-like signals in Section 3 and their impacts on the MJO-like disturbance's growth and/or propagation are discussed. Further discussion follows in section 4, with conclusions in section 5.

2. Model Description

a. SPCAM, forcing and Boundary Conditions

In this paper, we analyze output from SPCAM version 3.5. SPCAM is a modified version of the Community Atmosphere Model (CAM) where a small domain two-dimensional Cloud System Resolving Model (CSRM) is embedded within each grid point of CAM (Khairoutdinov and Randall, 2001; Khairoutdinov *et al.*, 2005). We use the version of SPCAM with semi-Lagrangian advection at T42 resolution for the CAM component. The model outputs have horizontal resolution of ~2.8 degrees. The embedded 2D CSRM is oriented in the north-south direction and has 32 grid points in the horizontal with a 4km resolution. There are 28 vertical levels in the CSRM aligned with the lower 28 vertical levels (out of 30) in the CAM model. The CAM time step is 15 minutes and the CSRM time step is 20 seconds.

The model is forced with a temporally and zonally constant Sea Surface Temperature (SST) given as a function of latitude ϕ, in degrees, by:

$$SST(\phi) = 2 + \frac{27}{2}(2 - \zeta - \zeta^2),$$

where the SST is in Celsius and

$$\zeta = \begin{cases} \sin^2\left(\pi \dfrac{\phi - 5}{110}\right) & 5 < \phi \leq 60 \\ \sin^2\left(\pi \dfrac{\phi - 5}{130}\right) & -60 \leq \phi < 5 \\ 1 & |\phi| < 60 \end{cases}$$

(plotted in figure 1a), and seasonally varying insolation for sixteen years, with output every three hours.

b. Simulated Climate

The model described produces a climate that is qualitatively similar to the central and east Pacific. Some interesting climate quantities are plotted in figure 1. The SST distribution used, which peaks at 5^oN, produces a single Inter-Tropical Convergence Zone (ITCZ) in the time mean, with strong precipitation peaked at around 5^oNorth (figure 1b), and secondary peaks in the storm tracks at around 40^o North and South.

The ITCZ is also the region of greatest column integrated water (WVP; figure 1c) and low-level zonal winds (U850; figure 1d) within the tropics. The U850 field shows easterlies throughout the tropics, with strongest winds on the edges of the ITCZ. The time/zonal mean low-level meridional wind is weak, but it shows convergence into the ITCZ and the tropics (not shown). The presence of the zonal easterlies in the tropics is a significant deviation from the climate in the region around the warm pool on Earth, where mean westerlies are observed. It is expected that, all else being equal, this will lead to surface flux anomalies that are significantly different to those on the Earth, as the sign of the WISHE effect is dependent upon the signs of both the mean state and anomalous winds. While the presence of a warm pool in the imposed SST can generate a more realistic wind distribution with zonal westerlies, we have chosen to use a simpler setup for this initial investigation.

While the low-level extra-tropical winds are stronger in the Northern Hemisphere, the Southern Hadley Circulation is stronger (not shown). The associated Southern jet is also stronger and more equatorial than the Northern one. This is consistent with the SST boundary condition and explains the strong SH extra-tropical anomalies. It is only at very low levels that the NH winds are slightly stronger.

c) *Moist Static Energy Calculation*

MSE (denoted by h) in our analysis will be defined as:

$$h = c_p T + gZ + L_v q - L_f q_i \qquad (1)$$

where T is temperature, c_p is the specific heat at constant pressure, Z is the height, g is the gravitational acceleration, L_v and L_f are the latent heats of vaporization and sublimation (at 0^{o}C), and q and q_i are the specific quantities of water vapor and ice respectively. This quantity is sometimes referred to as Frozen MSE. As constructed, the MSE is conserved under phase changes between the solid, liquid, and vapor phases of water and removal or addition of liquid water, all under hydrostatic motion. As a consequence, the column integral of h, $\langle h \rangle$, is approximately conserved in reality and in our model under convective adjustments. $\langle x \rangle$ represents the mass-weighted vertical integral of quantity x:

$$\langle x \rangle = \frac{1}{g} \int_{p_{top}}^{P_{surface}} x dp, \qquad (2)$$

where the integral runs from some defined top of the atmosphere (for sufficiently high tops, the results do not depend upon the precise value chosen) to the surface and g is the gravitational acceleration. The residual terms arising from non-MSE-conserving effects are generally small compared to other energy budget terms and can usually be neglected. (e.g. Neelin and Held 1987, Peters *et al.* 2008).

d) *Spectral Analysis of Model Fields*

The model equatorial precipitation shows a number of statistically significant peaks representing propagating disturbances (fig 2), when analyzed in zonal wavenumber-frequency space, just as observed in OLR from the satellite record (Wheeler and Kiladis 1999). These waves represent a large part of the tropical synoptic-scale convective variability, organizing individual convective elements (typically 100 km across, persisting for a few hours) into wavepackets with large spatial (thousands of kilometers) and temporal (days) scales (e.g., Chang 1970; Nakazawa 1988). The wave activity peaks have been identified with the equatorially trapped waves of rotating shallow water wave theories (e.g., Matsuno 1966; Wheeler and Kiladis 1999; Yang *et al.* 2007, Andersen and Kuang 2008). Not present in the classical shallow water wave system, and missing from most simple models is the large signal at intraseasonal (30-90 days) timescales and zonal wavenumbers 1-3 that is the spectral signal of the MJO.

Figure 2a shows the precipitation power spectrum for disturbances symmetric about the equator. This is constructed following the procedure of Wheeler and Kiladis (1999). These spectra are broadly similar to observations, with strong MJO, KW, and Rossby wave signals. The equivalent depth (a measure of the vertical scale of the wave structure, inferred from the phase speed) is approximately 25m, similar to that observed. SPCAM, with a generally similar SST distribution, has previously been shown to possess MJO-like spectral features (Marat Khairoutdinov, personal communication).

The antisymmetric part of the SPCAM spectrum (not shown) is not as realistic. For example, the Mixed Rossby-Gravity (MRG) waves are not well represented. However, we have observed that this feature is stronger in double ITCZ mean states. The mean state dependence of the features of the spectrum is an interesting and open question that we do not address here.

The spectrum of OLR (not shown) is generally similar. The spectra of MSE disturbances (figure 2b) are different to the precipitation and OLR spectra – the Kelvin and Rossby waves are weaker, while the MJO signal remains strong relative to the background (this is also seen in the observed spectra of precipitable water, e.g. Roundy and Frank 2004, Yasunaga and Mapes 2011). This is another indication that the MJO is a fundamentally different type of wave to the KW – one that is dominated by MSE fluctutions, rather than the buoyancy fluctuations that drive the shallow water wave type behaviour of the other waves. The MSE spectrum also includes a number of peaks around wavenumber 6. These are the signature of the strong extratropical waves present in our model entering the equatorial region. Care must be taken to exclude these waves from our MJO signatures used for the regression studies below.

In order to demonstrate that the column MSE anomalies are a fundamental part of the MJO-like disturbance rather than simply being generated by it, we have conducted an experiment where the column MSE in the model (between 20^{o}N-20^{o}S) is damped towards its time- and zonal-mean values with a 12-hour timescale. To maintain the climatology, the zonally averaging prognostic variables (excluding temperature) are nudged to the climatological values of the control runs over a timescale of 30 minutes. Temperature is nudged weakly with a timescale of 10 days. We have verified that nudging alone, without adding the column MSE damping, produced a spectrum similar to that of the control experiment. In this case, while the Kelvin waves are still present in the simulated precipitation, the MJO-like signal is greatly reduced (figure 2c). Figure 2d shows an experiment where radiative heating is homogenized in the zonal direction. The results of this experiment are discussed in below.

Figures 3a and figure 3b shows equatorial (0^o-6^oN) Hovmöller plots of precipitation for a short period of our model run. Even in the unfiltered field (figure 3a), a strong MJO event can be seen propagating eastwards, beginning at ~300E and Day 5600, continuing around the globe coherently for at least two full circumferences over a period of approximately 120 days. The multi-scale nature of the MJO in the model can be seen in this field - the MJO envelope contains and modulates many faster moving, short-lived waves traveling in both easterly and westerly directions.

Once the precipitation is filtered into the MJO frequency and wavenumber region of spectral space (wavenumbers 1—3, periods 20—100 days), the MJO signal is easily seen (figure 3b). MJO events tend to arise randomly, propagate for 1-2 circumnavigations and then die off, while another event arises elsewhere on the globe. The mechanisms involved in the events' beginnings and ends are beyond the scope of the current work and will not be investigated in this paper.

Poleward propagation can also be observed in the precipitation field. Figure 3c shows the time-latitude evolution of precipitation, averaged over 160^oE to 160^oW. Poleward propagating signals can be seen to move from near the equator to up to 25^oN.

3. Results

a) Regression Technique

To look at the structure of the MJO disturbances, we regress unfiltered model fields against the MJO filtered OLR field, with the following procedure:

1)Model OLR is filtered to the MJO spectral region $(1 \leq k \leq 3, 0.01/day \leq f \leq 0.05/\mathrm{day})$, in the fashion of Wheeler and Kiladis (1999), using a time-space Fourier transform followed by masking to the MJO region and then an inverse Fourier transform. The spectral region chosen is narrower than that used in Wheeler and Kiladis (1999) in order to reduce the contamination of the MJO signal by the very strong extra-tropical waves.

2)The time variance of the filtered OLR is calculated at each point and we identify the latitude that has the largest zonal mean variance – all of the reference points will come from this latitude. The reference latitude for the mean state considered is 4.2^oN, the location resolved with the model closest to the peak SST

*3)*We concatenate the filtered OLR time series for every point on the latitude chosen as our reference. This allows us to use the MJO from all parts of the globe to construct our regression improving the signal-to-noise, although it also introduces complications due to the various correlations in the fields.

*4)*The model fields are similarly concatenated into one long time series at each model point, appropriately circle shifted so that the spatial relationship with the reference points is maintained.

*5)*For each field of interest, at each spatial point in the model we estimate a regression coefficient, b – the slope of the model fields at that point versus the reference MJO OLR time series – using standard least-squares linear regression (e.g. Wilks 2006).

*6)*We consider the regression results statistically significant at each point if the null hypothesis ($b = 0$) can be rejected at the 95% confidence level for that point. For this purpose, we calculate confidence ranges for the slopes, by estimating the standard deviation, σ, of the population the slope is drawn from (again, through the standard techniques of least-squares linear regressions e.g. Wilks 2006). As there are time and space correlations in the various fields, we estimate the effective number of degrees of freedom (or independent MJO events) to be ~35000. This accounts for both the time correlations at each point and the spatial correlations between neighboring point's time series. We base this estimate upon observations of a correlation time of approximately 4 days and correlation length of approximately 8 degrees in the unfiltered fields such as zonal wind. We have also made estimates using the larger correlations in the filtered fields; this has little impact on the results that we present. We assume that the population of slopes has a Gaussian distribution, then the 95% confidence interval spans a region almost two standard deviations from the slope b:

$$b_{range} = b \pm 1.92 \times \sigma$$

Points where the null hypothesis cannot be sufficiently rejected are discarded.

7) The regression coefficients that pass the significance test are multiplied by a typical OLR peak anomaly (-40W/m^2), to give the magnitudes of the field anomalies associated with an MJO event.

This regression technique focuses on the mature phase of the MJO-like disturbance, which is, due to the zonal symmetry, the dominant phase in our model. The relationships between the model fields and the disturbance could be quite different during the initiation and decay phases of the disturbance.

b) *Dynamic field regressions*

The model fields are regressed against the MJO-filtered OLR on the latitude of greatest mean variance as described above to show the structure of the MJO-like disturbance in the model. Several model fields are shown in figure 4. The regression basis point at (180E, 4.2N) is indicated on the figures and the coastlines are included in the map to give a sense of the scale of the disturbances.

The composite MJO's convective signal can be seen in the OLR field (figure 4a) – which is essentially a measure of the average temperature of the highest opaque surface visible to the satellite. There is a large region of reduced OLR around the regression point, caused by colder emissions from the larger number of higher cloud tops in the active phase. The suppressed convection is visible as the warm anomalies, which are caused by the warmer temperatures of the low cloud tops and the greater lower-troposphere and sea surface area visible from space in this region.

Precipitation (figure 4b) is likewise enhanced near the regression point and suppressed to the east and west of the convective signal, although the enhancement is much stronger in the region of the ITCZ where the mean conditions are much more conducive to precipitation (and the mean precipitation is larger). The enhanced precipitation also possesses a noticeable tilt, with the eastern edge closer to the equator and the western edge closer to the pole. The convective region also contains a positive moisture anomaly, seen as an increase in the integrated column moisture (figure 4c), that has a tilt similar to the precipitation. The large moist anomalies in at around 120°W, 40°N and 40°S are due to the advection of moist tropical air by the MJO large-scale low-level winds. Similarly, the smaller dry anomaly at ~160°E, 30°S is due to the advection of dry extratropical air into the tropics by the MJO large-scale flow.

The OLR signal has a greater spatial extent than the precipitation. This is not considered surprising, as we expect that the OLR anomalies can be generated by modification in the amount or depth of convection throughout the tropics, while the precipitation anomalies are expected to be larger where the mean state conditions are more favorable for precipitation i.e. within the ITCZ.

The wind fields (850 hPa - figure 5a - and 200hPa - figure 5b) show circulation similar to that typical of the MJO, with low-level convergence near the convective center and divergence centered approximately halfway around the planet. The upper-level winds show a reversed pattern, with divergence above the reference point. The peak low-level winds are located near the ITCZ. While the westerlies peak to the west of the convective center, there is a small westerly signal under the convection. Also visible at low levels are the Rossby gyres associated with the MJO (e.g. Weickmann 1983, Hendon and Salby

1994, and Kiladis et al. 2005). However, the upper level gyre visible in the southern hemisphere is not the tropical response to the MJO heating. This gyre is located significantly closer to the equator, and the gyre is seen to tilt toward the pole with height, as seen in observations. In figure 5c, we can see the zonal wind structure at the reference longitude. The poleward tilt and the baroclinic nature of the gyre are visible near the equator. The gyre visible in the vector fields is due to the interaction with the extratropical response in the Southern jet, in the form of an equivalent barotropic gyre, which adds to the baroclinic tropical gyre to create the observed wind field.

The regressed fields also show strong signals of extra-tropical waves, present in the strong jets within the model. To the south of the equator, these signals can be quite prominent and quite equatorial due to the stronger southern Hadley Cell.

c) MSE budget and residual calculations

The MSE is calculated every three hours from the model instantaneous fields. The 3D MSE field and the column integrated MSE are regressed against the MJO index to give a composite structure of the MSE anomalies associated with the MJO. Much like observations of the Earth's MJO, the observed anomalies have a tilted vertical structure (figure 6a), with preconditioning of the lower and middle troposphere ahead (east) of the convective signal (Kiladis *et al.* 2005). This MSE anomaly is dominated in the low and middle troposphere by the moisture anomaly (not shown) associated with the signal. The peak MSE anomaly in the model is approximately 2 kJ/kg, in approximate agreement with observed values (e.g., Kemball-Cook and Weare 2001; Kiladis *et al.* 2005).

The column integrated MSE (figure 6b) closely follows the shape of the column integrated moisture field (Figure 4c) – as moisture anomalies dominate the column MSE anomalies at the MJO timescale – with a positive MSE anomaly running approximately along the ITCZ region, with the western end tilted polewards.

The column integrated MSE tendency is calculated in two ways. We can calculate it indirectly from the column integrated budget terms from the time mean fields over that three-hour interval:

$$\langle \partial_t h \rangle_{budget} = -\langle \omega \partial_p h \rangle - \langle v \cdot \nabla h \rangle + LH + SH + \langle LW \rangle + \langle SW \rangle, \tag{3}$$

where p is the pressure, v is the pressure-surface wind vector, ω is the pressure velocity, LH and SH represent the latent and sensible heat fluxes into the atmospheric column from the surface, and LW and SW are the long- and short-wave radiative heating rates. The left-hand side is the local tendency of $\langle h \rangle$, the first and second terms on the right represent advection of h by the winds, and the final four terms represent the external sources.

The MSE tendency can also be calculated directly by subtracting the MSE at the last time step from the current value before vertically integrating:

$$\langle \partial_t h \rangle_{explicit} = \langle \frac{h(t) - h(t - \Delta t)}{\Delta t} \rangle \tag{4}$$

Both these tendency terms are calculated explicitly from the eight times daily output of SPCAM and then regressed against the MJO OLR as described above, allowing us to determine their contributions to the MJO-like signal's MSE tendency.

The calculated budget for the MJO-like anomalies shows positive MSE tendencies to the east and to the north of the convective center with negative anomalies to the west and equatorwards. This distribution indicates that the MSE anomaly is propagating to the east and towards the pole (figure 6c).

The difference between the two $\langle \partial_t h \rangle$ values is the residual, and is a combination of numerical effects, processes that slightly violate conservation of MSE, and errors due to phenomena happening at time- and space-scales smaller than the scales in the output data. The residual is also regressed against the MJO OLR to determine its contribution to the MSE budget for the MJO (Figure 6d). For the small number of points where it is statistically significant, the regressed residual is generally small compared to the leading h tendency terms, allowing us to have some confidence in our diagnosis of these terms' contribution to the MSE budget for the MJO.

d) Decomposition

By projecting anomalies in the budget quantities onto the MSE anomaly and its time derivative, we can determine which terms contribute most to the maintenance/dissipation of the anomaly and which contribute to/retard the propagation. In figure 7a, the fractional energy source for the MSE anomaly due to each term is displayed (sensible heat flux is negligible and not plotted). The contribution due to source x, S_x, is calculated as

$$S_x = \frac{\|x \cdot \langle h \rangle\|}{\|\langle h \rangle^2\|}$$

where $\|y\| = \iint_{ITCZ} y dA$ is the integral over the ITCZ (6^{o}S to 12^{o}N here, along all longitudes) of quantity y. In this case, the "ITCZ" is defined as the region where precipitation is both strong and varies approximately linearly with column MSE.

From this we can see, firstly, that the MSE tendency is almost exactly in quadrature with the MSE anomaly, which is to be expected from the fashion in which we constructed the composites. We can also see that the long-wave heating, $\langle LW \rangle$, is the dominant source of column MSE for the MJO, with a small contribution from the short-wave heating, $\langle SW \rangle$, and the residual processes. The other terms shown - horizontal advection, $\langle \vec{V} \nabla h \rangle$, vertical advection, $\langle \omega \partial_p h \rangle$, and the latent heat flux, LHF, are all net sinks of column MSE. The sum of the sources is shown, for comparison with the projection of dh/dt. The difference is negligible compared to the sources shown.

The contribution each term x makes to the propagation, s_x, is shown in figure 7b. This is calculated in a similar way to the contribution to the anomaly:

$$s_x = \frac{\| x \cdot \langle dh/dt \rangle \|}{\| \langle dh/dt \rangle^2 \|}$$

As can be seen, the long-wave is the only significant retarding quantity, while both advection terms are significant sources of MSE associated with the propagation of the anomaly.

Comparison of the amplitude of the regression coefficients in the MSE budget (equation 3) allows us to identify the leading terms in the MJO MSE budget for this experiment. These are:

i. Long-wave heating (figure 8a) – The long-wave heating anomaly, caused primarily by the anomalously low OLR from the enhanced anvil clouds, acts as a source of column integrated MSE variability, balanced against the sinks due to the vertical and horizontal advection and latent heat flux anomalies in the region around the convective center. The long-wave heating anomaly is approximately 26% of the precipitation anomaly (in power units) at the regression point, larger than that observed by Lin and Mapes (2004). To demonstrate the importance of the long-wave heating to our observed anomaly, we have conducted a mechanism denial experiment, wherein the radiative heating is homogenized zonally, while the climatology is maintained through the same methods as the MSE damping experiment described above. In this case (figure 2d), we observe that the Kelvin waves are still active, while the MJO-like disturbance is absent from the precipitation spectrum.

ii. Horizontal advection (figure 8b) – Horizontal advection acts as a source of column MSE to the east and especially polewards of the convective center. The horizontal advection term is discussed in more detail below.

iii. Vertical advection (figure 8c) – Vertical advection of MSE appears to be a source of column integrated MSE to the east of the convective center, in the suppressed region, and a sink of column MSE in the convective region. This causes it to act as a damping on the anomaly. There is also a significant overlap between the vertical advection and the column MSE tendency, contributing to the eastward propagation. Vertical advection also appears to act against the polewards propagation, by counteracting some of the energy import by horizontal advection in the region polewards of the convective center. The Normalized Gross Moist Stability (NGMS) is defined as

$$NGMS = \frac{\langle \omega \partial_p h \rangle}{P},$$

where P is the precipitation anomaly in power units. For the composite disturbance in SPCAM, the NGMS at the regression point is approximately 0.21. NGMS is a measure of the efficiency with which the divergent flow exports MSE. A positive value represents stability, although a small value is more easily overcome by other mechanisms, such as the long-wave heating discussed previously. The NGMS could decrease with horizontal wavelength (e.g. Kuang 2011), contributing to the scale selection of the MJO-like distrubances. Whether this wavelength dependence is the case in our present experiments is not clear.

The column integrated MSE variability source represented by the advection at around 30^o to 40^oN is substantially polewards of the MSE tendency – this appears to be a signal of the extratropical waves that are strong in this model, rather than the MJO. The extratropical waves appear at the northern edge of the analysis domain as large signals in horizontal and vertical advection. These sources mostly cancel together as shown by the total advection, in figure 8d.

Surface latent heat flux (figure 9a) has a small contribution to the MSE anomaly propagation. However, as latent heat flux anomaly is a significant sink of column integrated MSE variability from the anomaly, this term deserves some investigation. The LHF anomaly is mostly negative under the positive column MSE anomaly, leading to damping of the MJO by LHF. This is not totally consistent with the simple WISHE picture and the mean state easterlies that exist near the equator.

The latent heating distribution observed can be explained in terms of a bulk surface flux formulation, which is a reasonable approximation for the surface scheme used in

SPCAM,

$$LHF = C\,\overrightarrow{|u|}\,\left(q^{*} - q_{sfc}\right), \tag{5}$$

where C is a constant; $\overrightarrow{|u|}$ is the windspeed near the surface; q^{*} is the saturation humidity at the surface temperature and pressure; and q_{sfc} is the actual humidity near the surface. In the WISHE argument, the changes in $\overrightarrow{|u|}$ across a disturbance are assumed to dominate changes in LHF. The climate-zonal mean latent heat flux calculated with equation 5 is qualitatively the same as that calculated by the model surface scheme (not shown). In this calculation, C is estimated by finding the multiplier that minimizes the difference between the two time-zonal mean LHF curves.

In the bulk surface flux calculation, the flux anomalies can be linearly approximated by a sum of flux anomalies due to the various anomalies in the dynamic fields associated with the MJO:

$$LHF \approx C\,\overrightarrow{|u|}\,\left(q^{*} - q_{sfc}\right) + C\Delta\,\overrightarrow{|u|}\,\left(q^{*} - q_{sfc}\right) - C\,\overrightarrow{|u|}\,\left(\Delta q_{sfc}\right) + C\,\overrightarrow{|u|}\,\left(\Delta q^{*}\right), \tag{6}$$

The first term on the right is the mean LHF, the second is the anomaly due to the changed wind speed as the MJO passes (figure 9b); the third term is the flux anomaly due to the change in moisture as the MJO passes (figure 9c) and the last term is the anomaly due to the change in surface saturation humidity due to the surface pressure anomalies of the MJO (not shown) which is negligible compared to the other terms.

As can be seen, the surface latent heat flux anomaly of the MJO is not purely determined by the wind speed anomaly. For example, the negative LHF anomaly to the northeast and southeast of the convection is dominated by the moisture anomaly due to the MJO scale circulation carrying moist equatorial air into the dryer regions outside the ITCZ. In these regions the wind speed anomalies are relatively small. On the other hand, the heating along the equator, west of the center, is largely due to the increased wind speed there, as the moisture anomaly near the surface is small in that region. As a third example, the weak negative anomaly to the west-northwest is due to the competition between a substantial slowing of the winds and a dry anomaly due to moisture advection. The reverse is also true to the east-north-east.

It is important to note that this decomposition should only be considered as a qualitative explanation of the flux anomalies, as the sum of the bulk flux derived anomalies does not match the actual flux anomaly quantitatively (compare figure 9a and figure 9d).

Due to the relative phases of the various terms, it appears that the propagation, especially the polewards part, is significantly driven by the horizontal advection of MSE, so we will now focus our attention on that term to gain further insight into the MJO propagation mechanisms.

e) Decomposition of horizontal advection into zonal and meridional advection:

While the advection in the model is Semi-Lagrangian, it can be approximately decomposed into zonal ($hadv_Z$) and meridional ($hadv_M$) contributions:

$$\begin{aligned} hadv_Z &= -\langle u \partial_x h \rangle \\ hadv_M &= -\langle v \partial_y h \rangle \end{aligned} \tag{7}$$

As can be seen in figure 10a, the zonal advection acts as a source of MSE to the northeast of the convective center. However, as discussed above, much of this MSE tendency is due to extratropical wave activity and is largely balanced by the vertical advection associated with the waves in the same area. The meridional MSE advection anomaly (figure 10b) also acts as a source of column integrated MSE to the east and to the northeast of the convective center and as a sink under the convective center and to equatorwards. This acts to propagate the MSE anomaly both eastwards and polewards.

f) Timescales of Meridional Advection

The meridional advection can be further divided into the contributions from various timescales:

$$-\langle v\partial_y h\rangle = -\langle v_{hf}\partial_y h_{hf}\rangle - \langle v_{lf}\partial_y h_{lf}\rangle - \langle v_{hf}\partial_y h_{lf}\rangle - \langle v_{lf}\partial_y h_{hf}\rangle \qquad (8)$$

where the subscripts *hf* indicates time filtered to periods $T < 30$ days; and *lf* indicates $T>30$ days.

Each of the four product terms is regressed against the MJO OLR signal. The dominant term, $-\langle v_{hf}\partial_y h_{hf}\rangle$, is shown in figure 10c. The remaining terms (not shown) are much less significant for the MJO-like signal. This figure shows a source of MSE to the northeast of the convective center, and a sink at the center, to the west, and to the northwest. This term dominates the total meridional advection to the energy source in the northeast, and so seems to dominate the polewards part of the propagation of the MJO-like signal and is a significant part of the eastward propagation.

The eddies in the model appear to act as a diffusion of MSE as we shall now show,

$$D \approx \kappa \nabla^2 \langle h \rangle,$$

where D is the diffusive source and κ is the eddy diffusion. To linear order, the eddy diffusion can be broken into the diffusion of the mean MSE profile by the MJO-associated eddy anomalies and the diffusion of the MJO MSE anomalies by the mean eddy activity. As a simple, dimensionally consistent, approximation, κ can be considered to be proportional to the square root of the Eddy Kinetic Energy (EKE):

$$\kappa = \bar{\kappa} + \kappa' \propto (\overline{EKE} + EKE')^{0.5}.$$

Expanding this to first order yields

$$\kappa' \propto \frac{1}{2} \frac{EKE'}{\overline{EKE}^{0.5}}.$$

The diffusion can then be written as:

$$D \propto \frac{1}{2} \frac{EKE'}{\overline{EKE}^{0.5}} \nabla^2 \overline{\langle h \rangle} + \overline{EKE}^{0.5} \nabla^2 \langle h \rangle',$$

where the primed quantities are associated with the MJO and the overbar indicates the climate mean quantities. These two quantities are shown as figures 11a and 11b. The first term is the diffusion of the mean MSE by the eddies associated with the MJO. The second term is the diffusion of the MJO MSE anomalies by the mean eddy activity.

As can be seen over the ITCZ latitudes, the MJO eddy term matches the meridional eddy MSE advection term to the east of the convection indicating that the MJO associated eddies are responsible for the meridional eddy advection in that region and thus provides the meridional advection's contribution to the eastward propagation. The mean eddy diffusion of the MSE anomaly, on the other hand, seems to be responsible for the advection to the north-east of the convection. Thus the gradients in the MJO MSE anomaly drive the poleward propagation of the MJO. The sum of the two diffusion terms is shown in figure 11c. The close correspondence between this and the eddy meridional advection (figure 10c) demonstrates the validity of representing the eddy advection terms as eddy diffusion, also shown to be the case in reanalysis data (Peters *et al.* 2008).

On the whole, what we seem to be seeing is a suppression of high-frequency eddy drying in the lower troposphere to the east of the convective center, and enhancement of the eddy drying to the west (figure 12a), in combination with MSE anomalies interacting with the mean eddy activity to create moistening to the northeast of the convection and drying near the convection. The vertical structure of the EKE anomaly (figure 12b) at 15^{o}N shows the suppression of eddy advection in the lower troposphere ahead of the convection, collocated with the anomalous moistening. Likewise, a positive EKE anomaly is collocated with anomalous drying. A similar picture emerges at 5^{o}N, where the anomalous moistening is closely tied to the suppressed EKE (figures 12c & 12d).

Figure 13a shows the 850hPa EKE anomaly, which can be seen to have a strong negative relationship to the column eddy meridional moisture advection anomaly (figure 10b). This relationship generally holds for the lower troposphere. The upper-level EKE anomalies generally have the opposite sign to the lower troposphere, but as the moisture gradient in the upper atmosphere is very small, the advection anomalies from the upper troposphere have a negligible influence upon the column integrated MSE. This is in agreement with observations of the eddy activity in the tropics, where the eddy kinetic energy is reduced in the MJO easterlies and enhanced in the MJO westerlies, dominated by barotropic conversion terms (e.g. Maloney and Hartmann 2001, Maloney and Dickinson 2003). Barotropic conversion moves mean flow energy into eddy energy, caused by eddy advection of gradients in the large-scale winds. The tendency of EKE due to barotropic conversion is given by

$$\partial_t EKE_{barotropic} = -u_{hf}v_{hf}\left(\partial_y u_{lf} + \partial_x v_{lf}\right) - u_{hf}^2\partial_x u_{lf} - v_{hf}^2\partial_y v_{lf} \tag{9}$$

where (u_{hf}, v_{hf}) is the high frequency wind and (u_{lf}, v_{lf}) are the low frequency winds. Figure 13b shows the MJO regressed generation of EKE by barotropic conversion (the right-hand side of the above equation), also at 850 hPa. As can be seen, extra EKE is generated by barotropic conversion in region around the convective center and to the west and northwest. EKE is reduced by the negative barotropic conversion anomaly in the region to the east of the convective center, consistent with the observations (e.g. Maloney and Hartmann 2001, Maloney and Dickinson 2003).

4. Discussion

Many attempts have been made to explain the tropical OLR spectrum as coming from a system of convectively coupled shallow water waves. However, the current results take the view that the MJO disturbance is of a fundamentally different nature, stemming from anomalies in column MSE, rather than from anomalies in Convective Available Potential Energy (CAPE) and/or other similar quantities caused by the temperature anomalies of the waves, as seems to be the case for the convectively-coupled equatorial shallow water waves observed.

To correctly model the MJO, it appears that a simple model must account for these effects. More specifically, because the horizontal advection of MSE due to meridional winds – and anomalies in this caused by variations in barotropic conversion – appears to have such a significant effect on the MJO mode, both the influence of these anomalies on the convection and the feedback on these effects by the large-scale flow induced by the MJO convection ought to be included.

We have also observed that surface thermodynamic disequilibrium caused by moisture anomalies can be as important as windspeed anomalies in determining the LHF anomalies, at least in the situation modeled in this study.

It is worthwhile discussing the ways our results compare to some other investigations of the MJO energy sources.

In a modeling study Raymond (2001) investigated the importance of cloud-radiation feedback and surface energy fluxes in the genesis and propagation of the MJO. Raymond observed that Cloud-Radiation feedback was crucial for MJO genesis, while surface heat fluxes were important for propagation. In the present analysis we do not investigate the genesis of the MJO events, but we do observe that cloud-radiation interactions (in the form of long-wave heating anomalies) are a major part of the MSE budget for the maintenance of the disturbance. Surface heat fluxes do not play a significant role in the propagation of the MJO-like anomaly we observe.

Raymond also observes that a mean state similar to that above the warm pool is critical to the existence of the MJO. However, we have observed the MJO in our zonally symmetric SPCAM experiment. It is not clear whether this observation is a strength or a weakness of SPCAM.

Lin and Mapes (2004) investigated the radiation budget of the MJO based upon observations from the Atmospheric Radiation Measurement (ARM) program and the Tropical Ocean Global Atmosphere Coupled Ocean Atmosphere Response Experiment (TOGA COARE) campaign. They observed that the net column radiative heating is almost in phase with the precipitation. We observe a similar phase relationship in SPCAM, where the radiative heating is approximately in phase with the MSE anomaly, with a slight lag indicated by the retarding effect of the long wave term. In both Lin and Mapes and the present work, the radiative heating anomaly is dominated by the long wave anomaly that results from changes in the high clouds by the MJO modulation of convection. The ratio of radiative heating to latent heat release we determine (26%) is significantly larger than the 15% estimated by Lin and Mapes.

Our results are generally consistent with those of Maloney (2009). We see a buildup of column MSE in advance of the precipitation anomaly and a decay of column MSE during and after the precipitation. We also observe that the horizontal advection of MSE is among the leading terms in the column MSE budget. However, in contrast to Maloney (2009), we observe that latent heat flux has only a small budget contribution. The long-wave heating anomaly is observed to be more important in the present work than it appears to be in Maloney 2009.

Our investigation of the mechanisms by which the horizontal advection terms operate is largely in agreement with that of Maloney 2009. The horizontal advection is dominated by the meridional transport of moisture by synoptic scale eddies. The modulation of the eddy activity by the MJO large-scale state leads to modulation of the moisture transport, leading to anomalous moistening and drying effects.

However, in a follow up paper, Maloney *et al*. (2010) made a number of observations that are inconsistent with the results we report. Specifically Maloney *et al*. reports that, in the presence of reduced humidity gradients (i.e. reduced eddy meridional advection effects) and a warm pool SST, the MJO observed is stronger. They further observed, in this configuration, that the propagation of the MSE anomaly was primarily due to zonal advection of moisture by the mean low-level wind. It is important to note, however, that the mean surface westerlies in Maloney et al. (2010) are considerably stronger than those observed over the Indian Ocean and the Western Pacific. We have not addressed the question of whether the mechanisms observed in SPCAM would change in a similar way in the present study, but this is a planned avenue of further research.

Poleward propagation of the MJO-like disturbance is demonstrated by the Hovmöller diagram in figure 3. This is not surprising, given the tilted nature of the MSE and precipitation anomalies. The MSE budgets indicate that meridional advection of MSE is important in the poleward propagation of the disturbance, and is likely important in the poleward propagation of similar phenomena on the Earth, such as the Asian Monsoon. In a study by Boos and Kuang (2010), similar poleward propagating intraseasonal anomalies are observed in a nonhydrostatic model with zonally symmetric boundary conditions. These anomalies are seen to propagate through a similar mechanism, through the actions of small scale eddies upon the column MSE.

5. Conclusions

By analyzing the column integral, we have glossed over the specifics of how moist convection in the model redistributes MSE. However, the budget analysis provides a useful framework to assess the importance of various processes. Our arguments, based upon budget analysis, are not intended to show causality. We can, however, see terms that are "important" in various parts of the wave, in the sense that, an important part of the budget is one that would necessitate large changes in the other terms to maintain balance were that term removed. It is also possible to infer from the signs of the important terms some information about how the MSE anomaly would react if a term was removed (eg, moving faster or slower, growing or decaying), at least in a transient sense, before the other terms responded.

Our conclusions are:

a) The SPCAM run in a zonally symmetric aquaplanet configuration shows an MJO-like feature in both the OLR and MSE spectra.

b) This feature is similar to the Earth's MJO in structure and propagation. The composite structure of the MJO-like signal shows enhanced moisture and precipitation in the convectively active region, coupled with a planetary scale circulation. The convective anomaly is preceded by low-level moistening, preconditioning the atmosphere for the convective activity. The anomalies propagate both eastwards at a realistic zonal speed and also polewards, similar to observations.

c) There are, however, some aspects of the disturbance that are less like the real-world MJO. Such differences are not surprising in an experiment conducted on an idealized zonally asymmetric aquaplanet set up, but we consider the system worth analyzing. The observation of realistic MJO events observed in experiments conducted in the same model with realistic boundary conditions, lends some confidence that our anomaly is related to the MJO, despite the differences. We believe that the analysis of this idealized experiment can be informative as to the mechanisms that are involved in the MJO maintenance and propagation.

d) The composite MJO-like feature appears as a large positive MSE anomaly located over and around the ITCZ and the center of MJO filtered OLR variability. The composite MSE tendency has MSE increasing to the east and polewards of the convective center, and decreasing to the west and equatorwards.

e) The primary source of MSE in phase with the observed anomaly is the anomalous long-wave heating, caused by the enhanced deep convection (and reduced mean cloud top/emission temperature) in the convective region of the MJO. This source of energy is balanced by sinks, which are dominated by the advection of MSE. The importance of long wave heating appears to be consistent with other investigations of MJO like oscillations, such as Hu and Randall (1994) and Raymond 2001. The importance of <LW> is confirmed by a mechanism denial experiment. When the radiative heating is homogenized zonally, the MJO-like disturbances disappear.

f) The latent heat flux anomalies associated with the MJO in our model are driven by both surface moisture anomalies and wind speed anomalies, contrary to the typical understanding of WISHE. Latent heat flux is also shown to be relatively unimportant to both the maintenance and the propagation of the MJO-like disturbance, in the sense of having only a small contribution to the MSE energy budgets either in phase or in quadrature with the MSE anomaly. The relative unimportance of LHF in our energy budget is in direct contradiction to many studies that have observed LHF playing an important role in the MJO, such as Maloney (2009) and Maloney *et al.* (2010).

g) The MSE sources associated with Eastward propagation of the anomaly are dominated by to the combined actions of the horizontal and vertical advection of MSE, which together create a positive MSE tendency ahead of the convective center and a negative one over and behind it, retarded by the long-wave heating.

h) The MSE sources associated with poleward propagation are dominated by the effect of horizontal advection of MSE, creating a positive tendency to polewards and to the east of the convective center and a negative tendency to the west and towards the equator. This advection is dominated by the meridional advection by high frequency eddies – anomalous moistening ahead of the convection due to suppression of eddy activity in this region – as observed by Maloney 2009. The robustness of this result across several different modeling studies speaks of its possible importance to the MJO on the Earth. Further, the good fit between our parameterized eddy diffusion and the eddy meridional advection indicates the validity of such a treatment.

i) The eddy advection, parameterized as diffusion, can be linearly approximated as the sum of diffusion of the mean MSE by eddy anomalies and the diffusion of the anomalous MSE by the mean eddies. The first quantity is seen to act as a source of MSE associated with the eastward propagation, while the second dominates the MSE sources associated with polewards propagation.

j) The eddy modulation is consistent with the modulation of barotropic conversion in the lower troposphere, due to the combined large-scale flow of the MJO and the mean state − suppressing conversion to the northeast and enhancing it to the north-west.

k) The absence of an interactive ocean or an ENSO cycle in our model does not preclude these mechanisms having an important role in the Earth's MJO. However, the observation of the MJO in our fixed SST experiment does imply that SST anomalies are not critical to the existence and propagation of MJO-like disturbances.

Such is the nature of the current understanding of the MJO that the observations reported here are consistent with (parts of) some studies and at odds with others. For example, our results generally contradict those of Raymond (2001) regarding the importance of latent heat flux while confirming the importance of cloud-radiation feedback. Our results are also in agreement with Lin and Mapes (2004) regarding the role of cloud-radiation feedback for the maintenance and propagation of the disturbance; and Maloney (2009) on the importance of the meridional eddy advection of MSE for the propagation of the anomaly. Investigation of the dependence of the budget upon the mean state in the style of Maloney *et al.* (2010) is beyond the scope of the current study, as we have limited our discussion to a single mean state. However, the response of the observed mechanisms in SPCAM to variations in the mean state is an avenue of research that we intend to pursue. Specifically, we will be analyzing how the balance between the budget terms varies with ITCZ width.

Acknowledgements:

The authors thank Marat Khairoutdinov and the CMMAP team for making the SPCAM model available; George Kiladis and an anonymous reviewer for their useful comments during the review process; and Mary Moore and Ji Nie for providing valuable feedback on drafts of this paper. This research was supported by NSF grant ATM-0754332. The Harvard Odyssey cluster provided the computing resources for this study.

References

Agudelo, P. A., J. A. Curry, C. D. Hoyos, and P. J. Webster, 2006: Transition between suppressed and active phases of intraseasonal oscillations in the Indo-Pacific warm pool. *J. Climate*, **19**, 5519–5530.

Andersen, J. A. and Z. Kuang, 2008: A Toy Model of the Instability in the Equatorially Trapped Convectively Coupled Waves on the Equatorial Beta Plane, *J. Atmos. Sci.*, **65**, 3736-3757.

Anyamba, E., E. Williams, J. Susskind, A. Fraser-Smith, and M. Fullekrug, 2000: The manifestation of the Madden-Julian Oscillation in global deep convection and in the Schumann resonance intensity, *J. Atmos. Sci.*, **57**, 1029–1044.

Araligidad, N. M., and E. D. Maloney, 2008: Wind-driven latent heat flux and the intraseasonal oscillation. *Geophys. Res. Lett.*, 35, L04815

Back, L. E., and C. S. Bretherton, 2005: The relationship between wind speed and precipitation in the east Pacific ITCZ. *J. Climate*, 18, 4317–4328.

Back, L. E., and C. S. Bretherton, 2006: Geographic variability in the export of moist static energy and vertical motion profiles in the trop- ical Pacific. *Geophys. Res. Lett.*, 33, L17810.

Benedict, J., and D. A. Randall, 2007: Observed characteristics of the MJO relative to maximum rainfall. *J. Atmos. Sci.*, **64**, 2332–2354.

Blade, I., and D. L. Hartmann, 1993: Tropical intraseasonal oscillation in a simple nonlinear model, *J. Atmos. Sci.*, 50, 2922– 2939.

Bond, N. A. and G. A. Vecchi, 2003: The Influence of the Madden–Julian Oscillation on Precipitation in Oregon and Washington. *Wea. Forecasting*, **18**, 600-613

Boos, W. R. and Z. Kuang, 2010: Mechanisms of poleward-propagating, intraseasonal convective anomalies in cloud-system resolving models. *J. Atmos. Sci.*, **67**, 3673-3691.

Bretherton, C. S., M. E. Peters, and L. E. Back, 2004: Relationships between water vapor path and precipitable water over the tropical oceans. *J. Climate*, 17, 1517–1528.

Brown, R. G., and C. Zhang, 1997: Variability of midtropospheric moisture and its effect on cloud-top height distribution during TOGA COARE. *J. Atmos. Sci.*, **54**, 2760--2774

Chang, C. P., 1970: Westward-propagating cloud patterns in the tropical Pacific as seen from time-composite satellite photographs. *J. Atmos. Sci.*, 27:133–138.

Derbyshire, S. H., I. Beau, P. Bechtold, J. -Y. Grandpeix, J. -M. Piriou, J. -L. Redelsperger, and P. M. M. Soares, 2004. Sensitivity of moist convection to environmental humidity. *Q. J. R. M. S.*, **130**, 3055--3079.

Emanuel, K. A., 1987: An air-sea interaction model of intraseasonal oscillations in the tropics, *J. Atmos. Sci.*, 44, 2324–2340.

Emanuel, K. A., J. D. Neelin, and C. S. Bretherton, 1994: On large-scale circulations in convecting atmospheres. *Q. J. R. M. S.*, **120**, 1111-1143

Ferranti, L., T. N. Palmer, F. Molteni, and E. Klinker 1990: Tropical-extratropical interaction associated with the 30 – 60 day oscillation and its impact on medium and extended range prediction, *J. Atmos. Sci.*, **47**, 2177–2199.

Frank, W. M., and P. E. Roundy, 2006: The relationship between tropical waves and tropical cyclogenesis. *Mon. Wea. Rev.*, **134**, 2397-2417.

Fuchs, Z., and D. J. Raymond, 2005: Large-scale modes in a rotating atmosphere with radiative–convective instability and WISHE. *J. Atmos. Sci.*, 62, 4084–4094.

Goswami, B. N., 2005: South Asian Summer Monsoon: An overview: in The Global Monsoon System: Research and Forecast Edited by C.-P. Chang, Bin Wang, Ngar-Cheung Gabriel Lau, Chapter 5, pp 47

Gutzler, D. S., and R. M. Ponte 1990: Exchange of momentum among atmosphere, ocean, and solid earth associated with the Madden-Julian Oscillation, *J. Geophys. Res.*, **95**, 18,679– 18,686.

Hall, J. D., A. J. Matthews, and D. J. Karoly 2001: The modulation of tropical cyclone activity in the Australian region by the Madden-Julian Oscillation, *Mon. Weather Rev.*, **129**, 2970– 2982.

Haertel, P. T., G. N. Kiladis, A. Denno, and T. Rickenbach, 2008: Vertical mode decompositions of 2-Day waves and the Madden Julian Oscillation. *J. Atmos. Sci.*, 65, 813-833.

Hendon, H. H. and B Liebmann, 1990: The Intraseasonal (30-50 day) Oscillation of the Australian Summer Monsoon. *Journal of the Atmospheric Sciences*, **47**, 2909-2923.

Hendon, H. H., B. Liebmann, M. E. Newman, J. D. Glick, and J. E. Schemm 2000: Medium-range forecast errors associated with active episodes of the Madden-Julian Oscillation, *Mon. Weather Rev.*, **128**, 69–86.

Hendon, H. H. and M. L. Salby, 1994. The Life Cycle of the Madden-Julian Oscillation, *J. Atmos. Sci.*, **51**, 2225-2237

Hidayat, R. and S. Kizu, 2010: Influence of the Madden–Julian Oscillation on Indonesian rainfall variability in austral summer, *Int. J. Clim.*, **30**, 1816-1825.

Higgins, R. W., and W. Shi, 2001: Intercomparison of the principal modes of interannual and intraseasonal variability of the North American monsoon system, *J. Clim.*, **14**, 403–417.

Hu, Q., and D. A. Randall, 1994: Low-frequency oscillations in radiative-convective systems, *J. Atmos. Sci.*, 51, 1089–1099.

Hu, Q., and D. A. Randall, 1995: Low-frequency oscillations in radiative-convective systems. Part II: An idealized model, *J. Atmos. Sci.*, 52, 478–490.

Jiang, X., T. Li, and B. Wang, 2004: Structures and Mechanisms of the Northward Propagating Boreal Summer Intraseasonal Oscillation. *J. Climate*, **17**, 1022–1039.

Johnson, R. H., T. M. Rickenbach, S. A. Rutledge, P. E. Ciesielski, and W. H. Schubert, 1999: Trimodal characteristics of tropical convection. *J. Climate*, 12, 2397–2418.

Jones, C., 2000: Occurrence of Extreme Precipitation Events in California and Relationships with the Madden–Julian Oscillation. *J. Climate*, **13**, 3576–3587.

Jones, C., and J.-K. E. Schemm 2000: The influence of intraseasonal variations on medium-range weather forecast over South America, *Mon. Weather Rev.*, **128**, 486–494.

Kemball-Cook, S. R., and B. C. Weare, 2001: The onset of convection in the Madden Julian Oscillation, *J. Climate*, 14, 780–793.

Khairoutdinov, M. F. and D. A. Randall, 2001: A cloud resolving model as a cloud parameterization in the NCAR Community Climate System Model: Preliminary results. *G. R. L.*, **28**, 3617--3620.

Khairoutdinov, M. F., D. A. Randall, and C. DeMott, 2005: Simulations of the atmospheric general circulation using a cloud-resolving model as a superparameterization of physical processes. *J. Atmos. Sci.*, **62**, 2136--2154.

Khouider, B., and A. J. Majda, 2006: A simple multicloud parameterization for convectively coupled tropical waves. Part I: Linear analysis. *J. Atmos. Sci.*, **63**, 1308--1323

Kikuchi, K., and Y. N. Takayuba, 2004: The development of organized convection associated with the MJO during TOGACOARE IOP: Trimodal characteristics. *Geophys. Res. Lett.*, 31, L10101.

Kiladis, G. N., K. H. Straub, and P. T. Haertel, 2005: Zonal and vertical structure of the Madden-Julian Oscillation. *J. Atmos. Sci.*, **62**, 2790-2809.

Kiladis, G. N., M. C. Wheeler, P. T. Haertel, K. H. Straub, and P. E. Roundy, 2009: Convectively coupled equatorial waves. *Rev. Geoph.*, **47**, 2008RG000266

Krishnamurti, T. N., D. Subrahmanyam, 1982: The 30–50 Day Mode at 850 mb During MONEX. J. Atmos. Sci., 39, 2088–2095.

Kuang, Z., and C. S. Bretherton, 2006: A mass-flux scheme view of a high-resolution simulation of a transition from shallow to deep cumulus convection. *J. Atmos. Sci.*, **63**, 1895--1909.

Kuang, Z., 2008: A Moisture-Stratiform Instability for Convectively Coupled Waves. *J. Atmos. Sci.*, **65**, 834--834.

Kuang, Z. 2011: The wavelength dependence of the gross moist stability and the scale selection in the instability of column integrated moist static energy, *J. Atmos. Sci.*, 68, 61-74.

Langley, R. B., R. W. King, I. I. Shapiro, R. D. Rosen, and D. A. Salstein, 1981: Atmospheric angular momentum and the length of the day: A common fluctuation with a period of 50 days, *Nature*, **294**, 730–732.

Lau, K.-M. and P. H. Chan, 1986: Aspects of the 40-50 day oscillation during the northern summer as inferred from outgoing longwave radiation. *Mon. Wea. Rev.*, **114**, 1354-1367.

Lau, K.-M., and L. Peng, 1987: Origin of low-frequency (intraseasonal) oscillations in the tropical atmosphere. Part I: Basic theory, *J. Atmos. Sci.*, **44**, 950–972.

Lau, K-M., L. Peng, 1990: Origin of Low Frequency (Intraseasonal) Oscillations in the Tropical Atmosphere. Part III: Monsoon Dynamics. *J. Atmos. Sci.*, **47**, 1443–1462.

Lau, K.-M. and H.-T. Wu, 2010: Characteristics of Precipitation, Cloud and Latent Heating Associated with the Madden-Julian Oscillation. *J. Climate.,* **23**, 504-518

Lau, K-M., C-H. Sui, 1997: Mechanisms of Short-Term Sea Surface Temperature Regulation: Observations during TOGA COARE. *J. Climate*, **10**, 465–472.

Lawrence, D. and P. J. Webster, 2002: The boreal summer intraseasonal oscillation and the South Asian monsoon. *J. Atmos. Sci.*, **59**, 1593-1606.

Leroy, A. and M. C. Wheeler, 2008: Statistical Prediction of Weekly Tropical Cyclone Activity in the Southern Hemisphere, *Mon. Wea. Rev.*, **136**, 3637-3657.

Liebmann, B., H. Hendon, and J. Glick, 1994: The relationship between tropical cyclones of the western Pacific and Indian oceans and the Madden-Julian Oscillation, *J. Meteorol. Soc. Jpn.*, **72**, 401–411.

Liebmann, B., and C. A. Smith, 1996: Description of a complete (Interpolated) outgoing longwave radiation dataset. *Bul. of the Amer. Meteorol. Soc.*, **77**, 1275-1277.

Liebmann, B, G. N. Kiladis, C. S. Vera, A. C. Saulo, and L. M.V. Carvalho, 2004: Subseasonal variations of Rainfall in South America in the Vicinity of the Low-Level Jet East of the Andes and Comparison to Those in the South Atlantic Convergence Zone. *Journal of Climate*, **17**, 3829-3842.

Lin, J.-L., and B. E. Mapes, 2004: Radiation budget of the tropical intraseasonal oscillation. *J. Atmos. Sci.*, **61**, 2050–2062.

Madden, R. A., and P. R. Julian 1971: Detection of a 40–50 day oscillation in the zonal wind in the tropical Pacific, *J. Atmos. Sci.*, **28**, 702–708.

Madden, R. A., and P. R. Julian 1972: Description of global-scale circulation cells in the tropics with a 40 – 50 day period, *J. Atmos. Sci.*, **29**, 1109–1123.

Madden, R. A., 1986: Seasonal variations of the 40 – 50 day oscillation in the tropics, *J. Atmos. Sci.*, **43**, 3138–3158.

Majda, A. and M. Schefter, 2001: Waves and instabilities for model tropical convective parameterizations, *J. Atmos. Sci.*, **8**, 896-941.

Maloney, E. D., and D. L. Hartmann, 1998: Frictional moisture convergence in a composite life cycle of the Madden-Julian Oscillation, *J. Clim.*, **11**, 2387–2403.

Maloney, E. D., and D. L. Hartmann 2000: Modulation of eastern North Pacific hurricanes by the Madden-Julian Oscillation, *J. Clim.*, **13**, 1451–1460.

Maloney, E. D., and D. L. Hartmann 2001: The Madden-Julian oscillation, barotropic dynamics, and North Pacific tropical cyclone formation. Part I: Observations, *J. Atmos. Sci.*, **58**, 2545–2558.

Maloney, E. D., and M. J. Dickinson, 2003: The intraseasonal oscillation and the energetics of summertime tropical western North Pacific synoptic-scale disturbances. *J. Atmos. Sci.*, **60**, 2153–2168.

Maloney, E. D., and A. H. Sobel, 2004: Surface fluxes and ocean coupling in the tropical intraseasonal oscillation. *J. Climate*, **17**, 4368–4386.

Maloney, E. D., and S. K. Esbensen, 2007: Satellite and buoy observations of boreal summer intraseasonal variability in the tropical northeast Pacific. *Mon. Wea. Rev.*, **135**, 3–19.

Maloney, E. D., 2009: The Moist Static Energy Budget of a Composite Tropical Intraseasonal Oscillation in a Climate Model. *J. Climate.*, **22**, 711–729.

Maloney, E. D., A. H. Sobel, and W. M. Hannah, 2010: Intraseasonal Variability in an Aquaplanet General Circulation Model. *J.A.M.E.S.*, **2**, 5.

Mapes, B. E., and P. Zuidema, 1996: Radiative-dynamical consequences of dry tongues in the tropical troposphere. *J. Atmos. Sci.*, **53**, 620–638.

Mapes, B. E., 2000: Convective inhibition, subgrid-scale triggering energy, and stratiform instability in a toy tropical wave model. *J. Atmos. Sci.*, **57**, 1515--1535.

Masunaga, H., T. S. L'Ecuyer, and C. D. Kummerow, 2006: The Madden–Julian oscillation recorded in early observations from the Tropical Rainfall Measuring Mission (TRMM). *J. Atmos. Sci.*, **63**, 2777–2794.

Matsuno, T., 1966: Quasi-geostrophic motions in the equatorial area. *J. Meteor. Soc. Japan*, **44**, 25–43.

Matthews, A. J., 2000: Propagation mechanisms for the Madden- Julian Oscillation, *Q. J. R. Meteorol. Soc.*, **126**, 2637–2651.

Matthews AJ, 2004: Intraseasonal variability over tropical Africa during northern summer. *J. Climate,* **17,** 2427-2440.

Mo, K. C. and R. W. Higgins, 1998: Tropical influences on California precipitation. *J. Climate*, **11**, 412-430.

Myers, D. S., & Waliser, D. E., 2003: Three-Dimensional Water Vapor and Cloud Variations Associated with the Madden-Julian Oscillation during Northern Hemisphere Winter. *Journal of Climate*, **16**, 929-950.

Nakazawa, T., 1988: Tropical super clusters within intraseasonal variations over the western Pacific, *J. Meteorol. Soc. Jpn.*, **66**, 823 – 836.

Neelin, J. D., and I. M. Held, 1987: Modeling tropical convergence based on the moist static energy budget. *Mon. Wea. Rev.*, **115**, 3–12.

Neelin, J. D., I. M. Held, and K. H. Cook, 1987: Evaporation- wind feedback and low-frequency variability in the tropical atmosphere, *J. Atmos. Sci.*, **44**, 2341–2348.

Nieto Ferreira, R., W. H. Schubert, and J. J. Hack, 1996: Dynamical aspects of twin tropical cyclones associated with the Madden-Julian Oscillation, *J. Atmos. Sci.*, **53**, 929–945.

Paegle, J. N., L. A. Byerle, and K. C. Mo, 2000: Intraseasonal modulation of South American summer precipitation. *Mon. Wea. Rev.*, **128**, 837-850.

Peters, M. E., and C. S. Bretherton, 2006: Structure of tropical variability from a vertical mode perspective. *Theor. Comput. Fluid. Dyn.*, **20**, 501–524, doi:10.1007/s00162-006-0034-x.

Peters, M. E., Z. Kuang, and C. Walker, Analysis of atmospheric energy transport in ERA40 and implications for simple models of the mean tropical circulation, 2008: *Journal of Climate*, **21**, 5229-5241

Peters, O., and J. D. Neelin, 2006: Critical phenomena in atmospheric precipitation. *Nature Phys.*, **2**, 393–396.

Raymond, D. J., 2000: Thermodynamic control of tropical rainfall. *Quart. J. Roy. Meteor. Soc.*, **126**, 889–898.

Raymond, D. J., 2001: A new model of the Madden–Julian oscillation. *J. Atmos. Sci.*, **58**, 2807–2819.

Raymond, D. J., G. B. Raga, C. S. Bretherton, J. Molinari, C. Lopez-Carrillo, and Z. Fuchs, 2003: Convective forcing in the intertropical convergence zone of the eastern Pacific. *J. Atmos. Sci.*, **60**, 2064–2082.

Redelsperger, J,-L., D. B. Parsons, and F. Guichard, 2002: Recovery processes and factors limiting cloud-top height following the arrival of a dry intrusion observed during TOGA COARE. *J. Atmos. Sci.*, **59**, 2438--2457.

Ridout, J. A., 2002: Sensitivity of tropical Pacific convection to dry layers at mid- to upper levels: Simulation and parameterization tests. *J. Atmos. Sci.*, **59**, 3362--3381.

Roca, R., S. Louvet, L. Picon, and M. Desbois, 2005: A study of convective systems, water vapor and top of the atmosphere cloud radiative forcing over the Indian Ocean using INSAT-1B and ERBE data. *Meteorol. Atmos. Phys.*, **90**, 49--65.

Roundy, P. E., and W. M. Frank, 2004: Climatology of Waves in the Equatorial Region. *J. Atmos. Sci.*, **61**, 2105--2132

Rui, H., and B. Wang, 1990, Development characteristics and dynamic structure of tropical intraseasonal convection anomalies, *J. Atmos. Sci.*, **47**, 357–379.

Salby, M. L., and H. H. Hendon 1994: Intraseasonal behavior of clouds, temperature, and winds in the tropics, *J. Atmos. Sci.*, **51**, 2207 – 2224.

Sherwood, S. C., 1999: Convective precursors and predictability in the tropical western Pacific. *Mon. Wea. Rev.*, **127**, 2977--2991.

Sikka, D. R. and S. Gadgil, 1980: On the maximum cloud zone and ITCZ over the Indian longitudes during the southwest monsoon. *Mon. Wea. Rev.,* **108**, 1122-1135.

Sobel, A. H. and H. Gildor 2003: A Simple Time-Dependent Model of SST Hot Spots. *J Climate*, **16**, 3978-3992.

Sobel, A. H., S. E. Yuter, C. S. Bretherton, and G. N. Kiladis, 2004: Large-scale meteorology and deep convection during TRMM KWAJEX. *Mon. Wea. Rev.*, **132**, 422–444.

Sobel, A. H., E. D. Maloney, G. Bellon, and D. M. Frierson, 2010: Surface Fluxes and Tropical Intraseasonal Variability: a Reassessment. *JAMES*, **2**, Article 2. DOI:10.3894/JAMES.2010.2.2

Stephens, G. L., P. J. Webster, R. H. Johnson, R. Engelen, and T. L'Ecuyer, 2004: Observational evidence for the mutual regulation of the tropical hydrological cycle and tropical sea surface temperatures. *J. Climate*, **17**, 2213–2224.

Sugiyama, M., 2009a: The Moisture Mode in the Quasi-Equilibrium Tropical Circulation Model. Part I: Analysis Based on the Weak Temperature Gradient Approximation. *J. Atmos. Sci.*, **66**, 1507–1523.

Sugiyama, M., 2009b: The Moisture Mode in the Quasi-Equilibrium Tropical Circulation Model. Part II: Nonlinear Behavior on an Equatorial β Plane. *J. Atmos. Sci.*, **66**, 1525–1542.

Sui, K. -H. and K. -M. Lau, 1992: Multiscale Phenomenon in the Tropical Atmosphere over the Western Pacific. *Mon. Wea. Rev.*, **120**, 407-430.

Takemi, T., O. Hirayama, and C. Liu, 2004: Factors responsible for the vertical development of tropical oceanic cumulus convection. *G.R.L.*, **31**, L11109.

Tian, B., D. E. Waliser, E. J. Fetzer, B. H. Lambrigtsen, Y. Yung, and B. Wang, 2006: Vertical moist thermodynamic structure and spatial–temporal evolution of the MJO in AIRS observations. *J. Atmos. Sci.*, **63**, 2462–2485.

Waliser, D. E., K. Weickmann, R. Dole, S. Schubert, O. Alves, C. Jones, M. Newman, H.-L. Pan, A. Roubicek, C. Smith, H. van den Dool, F. Vitart, M. Wheeler, J. Whitaker, 2006: The Experimental MJO Prediction Project. *Bull. American Meteo. Soc.*, **87**, 425-431

Wang, B., 1988: Dynamics of tropical low-frequency waves: An analysis of the moist Kelvin wave, *J. Atmos. Sci.,* **45**, 2051 – 2065.

Wang, B., and H. Rui, 1990a: Synoptic climatology of transient tropical intraseasonal convective anomalies: 1975 – 1985, *Meteorol. Atmos. Phys.*, **44**, 43–61.

Wang B., and H. Rui, 1990b: Dynamics of the Coupled Moist Kelvin-Rossby Wave on an Equatorial B-Plane. *J. Atmos. Sci*, **47**, 397-413

Wang, B. and X. Xie, 1997: A model for the boreal summer Intraseasonal Oscillation. *J. Atmos. Sci.*, **54**, 72-86.

Wang, W., and M. E. Schlesinger, 1999: The dependence on convection parameterization of the tropical intraseasonal oscillation simulated by the UIUC 11-layer atmospheric GCM. *J. Climate*, **12**, 1423–1457.

Webster, P. J., 1983: Mechanisms of Monsoon Transition: Surface Hydrology Effects. *J. Atmos. Sci.*, **40**, 2110-2124.

Weickmann, K. M., 1983: Intraseasonal Circulation and Outgoing Longwave Radiation Modes During Northern Hemisphere Winter. *Mon. Wea. Rev.*, **111**, 1838--1858.

Weickmann, K. M., G. N. Kiladis, and P. D. Sardeshmukh, 1997: The dynamics of intraseasonal atmospheric angular momentum oscillations, *J. Atmos. Sci.*, **54**, 1445–1461.

Wheeler, M. and G. N. Kiladis, 1999: Convectively Coupled Equatorial Waves: Analysis of Clouds and Temperature in the Wavenumber-Frequency Domain. *J.Atmos. Sci.,* ***56****, 374*–399.

Wilks D. S., 2006: Statistical Methods in the Atmospheric Sciences (2nd Ed.), Elsevier, pp 180-196

Woolnough, S. J., J. M. Slingo, and B. J. Hoskins, 2001: The organization of tropical convection by intraseasonal sea surface temperature anomalies. *Quart. J. Roy. Meteor. Soc.*, **127**, 887– 907.

Xie, P., and P. A. Arkin, 1997: Global precipitation: A 17-year monthly analysis based on gauge observations, satellite esti- mates, and numerical model outputs, *Bull. Am. Meteorol. Soc.*, **78**, 2539–2558.

Yanai, M, B Chen, W.-W Tung, 2000: The Madden–Julian Oscillation Observed during the TOGA COARE IOP: Global View. *J. Atmos. Sci.*, **57**, 2374–2396.

Yang, G-Y., B. Hoskins, and J. Slingo, 2007: Convectively coupled equatorial waves. Part I: Horizontal and vertical structures. *J. Atmos. Sci.*, **64**, 3406–3423.

Yasunaga, K., and B. E. Mapes, 2011: Differences between more-divergent vs. more-rotational types of Convectively Coupled Equatorial Waves. Part I: Space-Time Spectral Analyses. *J. Atmos. Sci., in press*

Yasunari, T., 1979: Cloudiness fluctuations associated with the Northern Hemisphere summer monsoon, *J. Meteorol. Soc. Jpn.*, **57**, 227–242.

Zhang, C., and H. H. Hendon, 1997: On propagating and stationary components of the intraseasonal oscillation in tropical convection, *J. Atmos. Sci.*, **54**, 741–752.

Zhang, C., 1996: Atmospheric intraseasonal variability at the surface in the western Pacific Ocean. *J. Atmos. Sci.*, **53**, 739–758.

Zhang, C., 2005: Madden-Julian Oscillation. *Rev. Geophys.*, **43**, RG2003.

List of Figures

FIG. 6. MJO regressed MSE and column MSE budget terms. a) Zonal-Vertical cross-section along the ITCZ peak; b) Column integrated MSE anomaly; c) Column integrated MSE time tendency; d) MJO regressed residual.

FIG. 7. a) Fractional contributions of the MSE budget terms to the maintenance/dissipation of the MJO MSE anomaly. b) Fractional contributions of the MSE budget terms to the propagation of the MJO MSE anomaly.

FIG. 8. Leading terms in the MJO regressed column MSE budget. a) Column integrated long wave radiation forcing; b) Column integrated horizontal advection of MSE; c) Column integrated vertical advection of MSE (equivalent to column integrated MSE convergence); d) Total column integrated advection of MSE.

FIG. 9. Latent Heating Terms. a) MJO regressed Latent Heat Flux Anomaly; b) MJO Latent Heating anomaly attributable to changes in surface level windspeed in a bulk surface flux calculation; c) MJO Latent Heating anomaly attributable to changes in surface level moisture content in a bulk surface flux calculation; d) Total bulk surface scheme latent heat flux anomaly.

FIG. 10. a) Column integrated zonal advection of MSE; b) Column integrated meridional advection of MSE; c) column integrated, MJO regressed, high frequency v-high frequency h advection.

FIG. 11. Eddy Diffusion of MSE anomalies. a) Diffusion of mean MSE by MJO eddy anomalies; b) Diffusion of eddy MSE anomalies by mean eddy activity; c) Total eddy diffusion of MSE. All figures are in arbitrary but consistent units.

FIG. 12. a) Anomalous Eddy Meridional Advection of MSE at N; b) Eddy Kinetic Energy (EKE) anomaly at N; c) Anomalous Eddy Meridional Advection of MSE at N; and d) Eddy Kinetic Energy (EKE) anomaly at N. MJO regression point is located at Note the differences in vertical scale between the first and second pair of figures.

FIG. 13. a) The MJO regressed EKE anomaly at 850 hPa; b) EKE source due to barotropic conversion of energy from the large scale winds at 850 hPa.

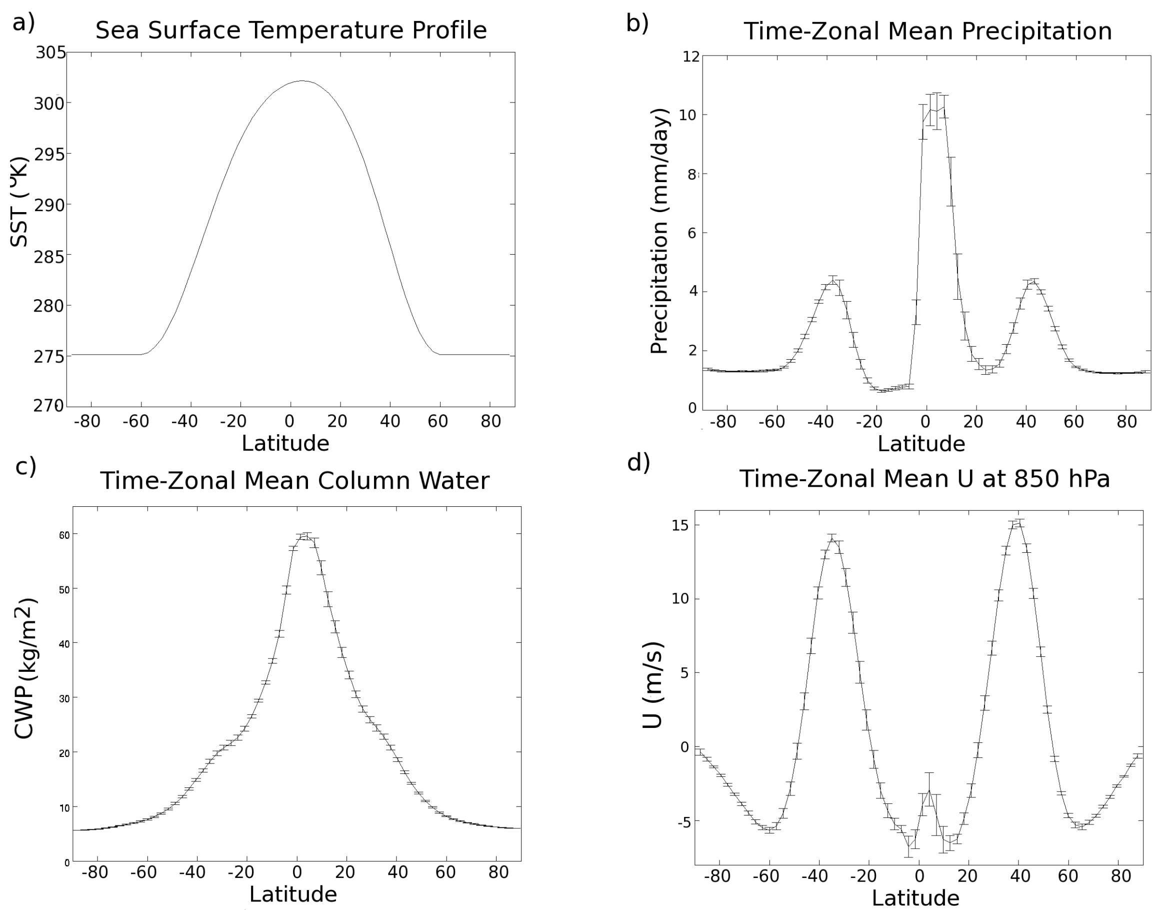

FIG. 1. Time and zonal mean climate: a) Sea Surface Temperature, b) Precipitation, c) Column Moisture, and d) 850hPa Zonal Wind. Error bars indicate the standard deviation of the zonal mean of the time mean values.

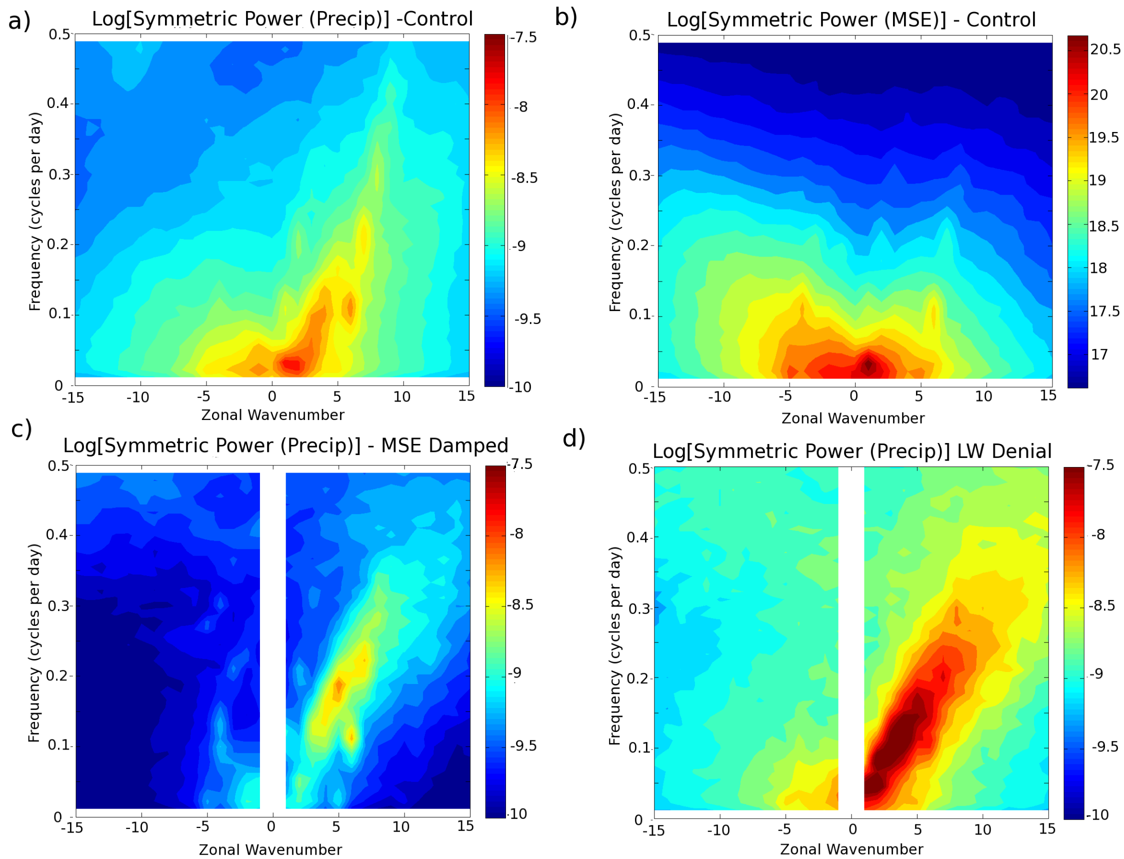

FIG. 2. Logarithm (base 10) of the spectral power for signals symmetric about the equator in a) precipitation, and b) MSE for the control case and precipitation for the c) MSE Damped and d) LW Denial cases. The power spectrum is averaged over the region 15°S to 15°N and is constructed from model output (after Wheeler and Kiladis 1999). The wavenumber zero data for panels c) and d) is deleted as it is rendered meaningless by the experimental procedure.

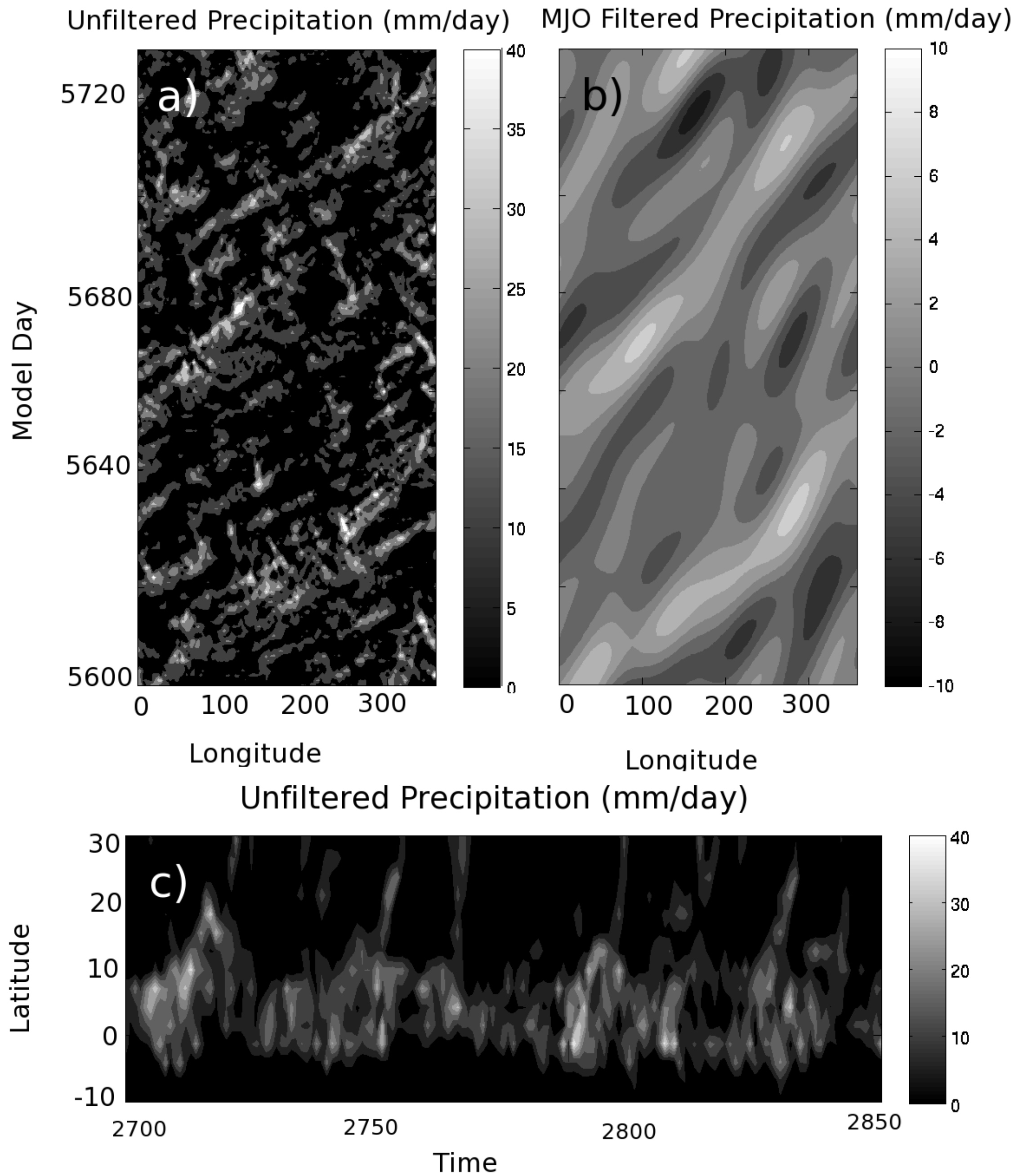

FIG. 3. Hovmöller diagrams a) Unfiltered precipitation signal (averaged over 0^{o}N-6^{o}N); b) MJO frequency-wavenumber filtered precipitation signal (averaged over 0^{o}N-6^{o}N); c) Unfiltered precipitation signal (averaged over 160^{o}E-160^{o}W);

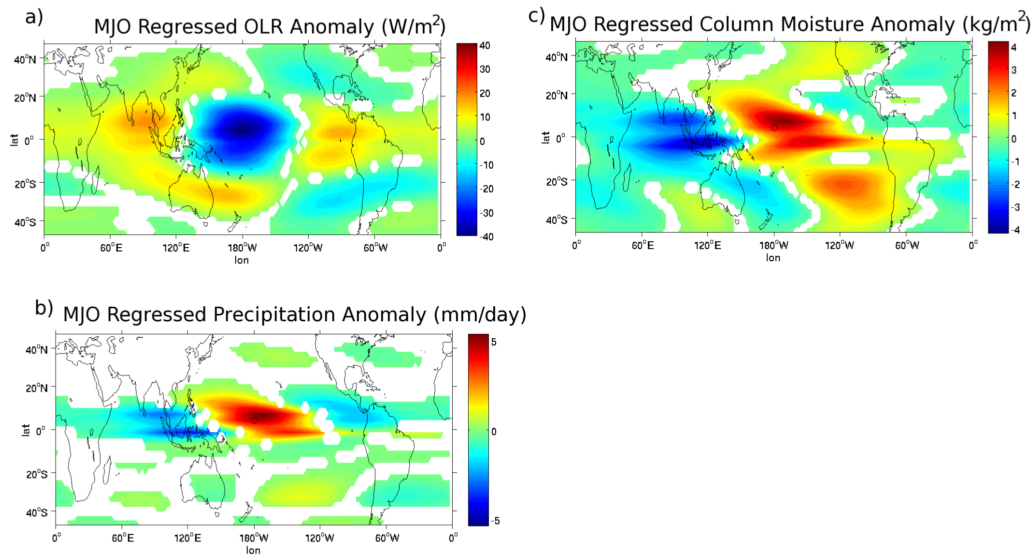

FIG. 4. Composite anomalies for the MJO like disturbances produced by regression, scaled to a -40W/m^2 OLR anomaly. a) Outgoing Long-wave Radiation; b) Precipitation; c) column integrated moisture.

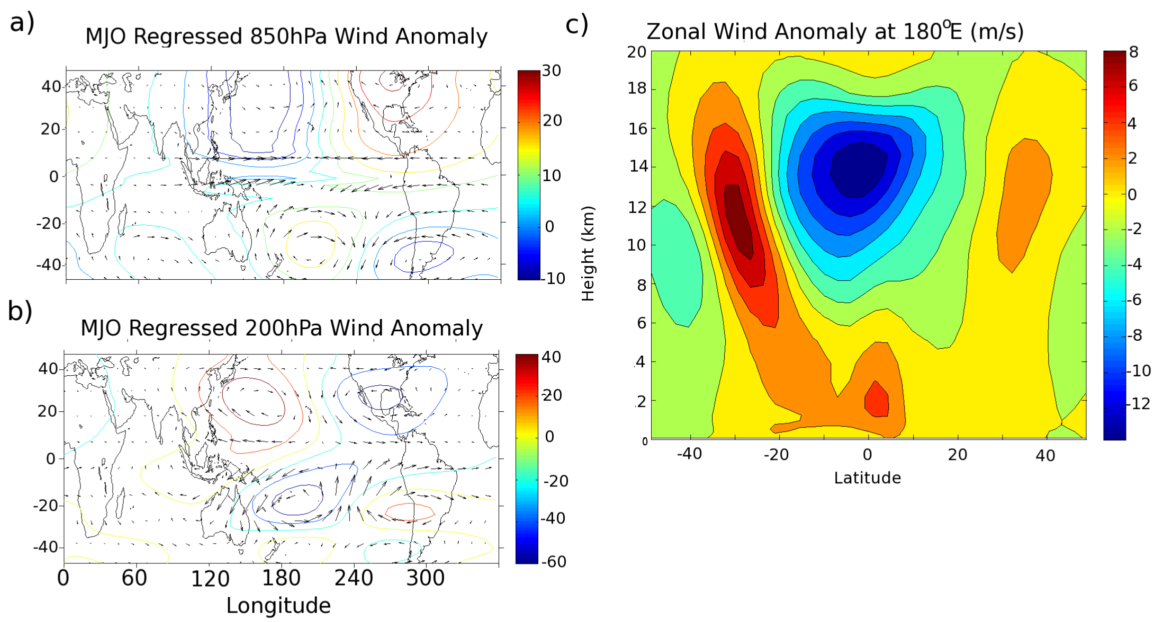

FIG. 5. Composite winds anomalies (vectors) for the MJO like disturbances produced by regression and stream function (contours), scaled to a -40W/m^2 OLR anomaly. a) 850hPa (maximum wind speed 5.1 m/s); b) 200hPa (maximum wind speed 11.2 m/s); c) Vertical-meridional cross section of MJO regressed zonal wind at the reference longitude.

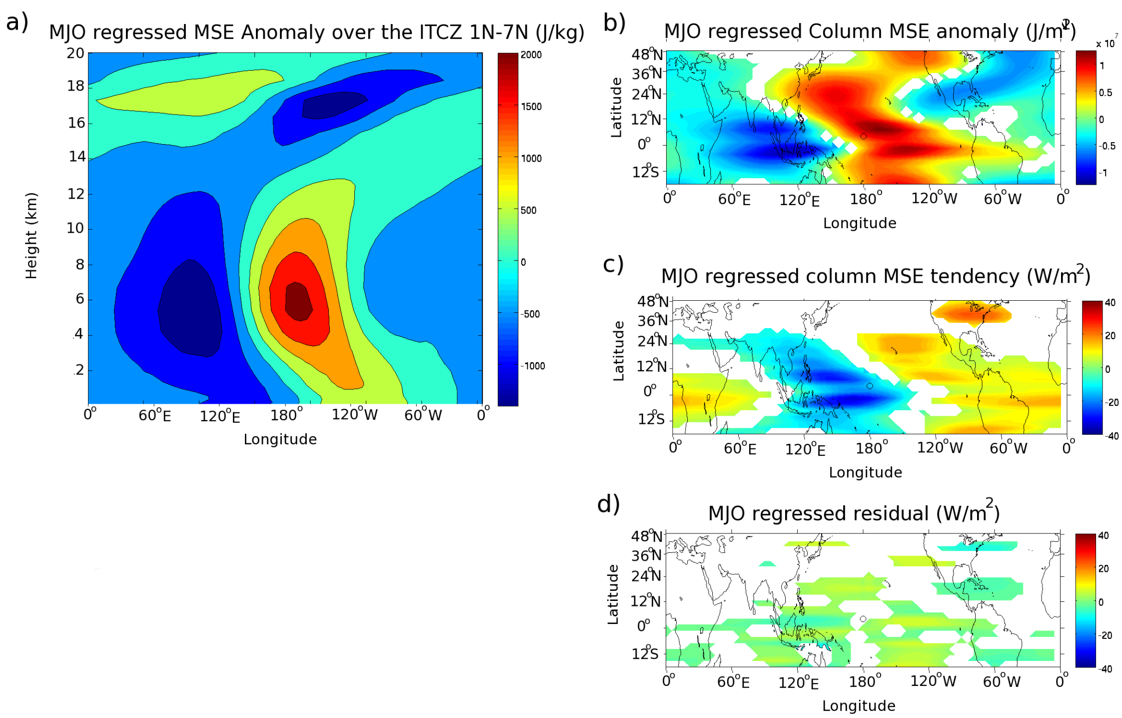

FIG. 6. MJO regressed MSE and column MSE budget terms. a) Zonal-Vertical cross-section along the ITCZ peak; b) Column integrated MSE anomaly; c) Column integrated MSE time tendency; d) MJO regressed residual.

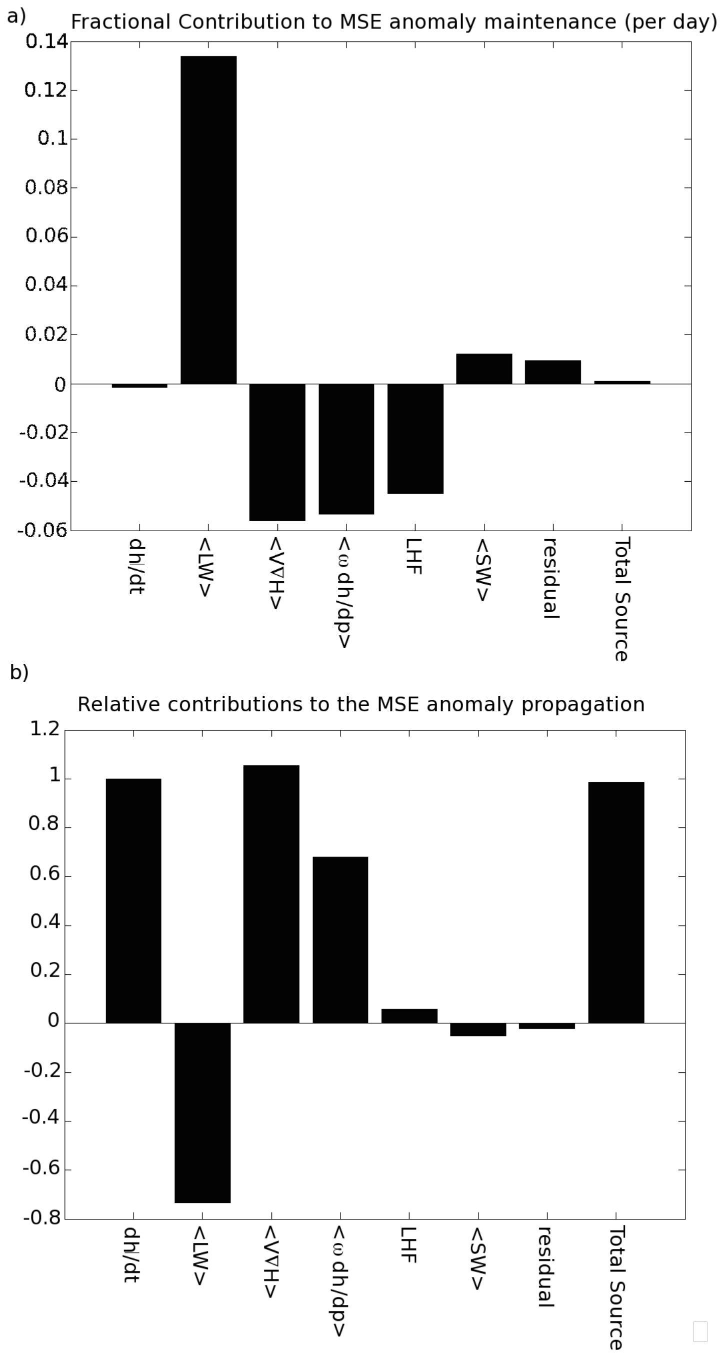

FIG. 7. a) Fractional contributions of the MSE budget terms to the maintenance/dissipation of the MJO MSE anomaly. b) Fractional contributions of the MSE budget terms to the propagation of the MJO MSE anomaly.

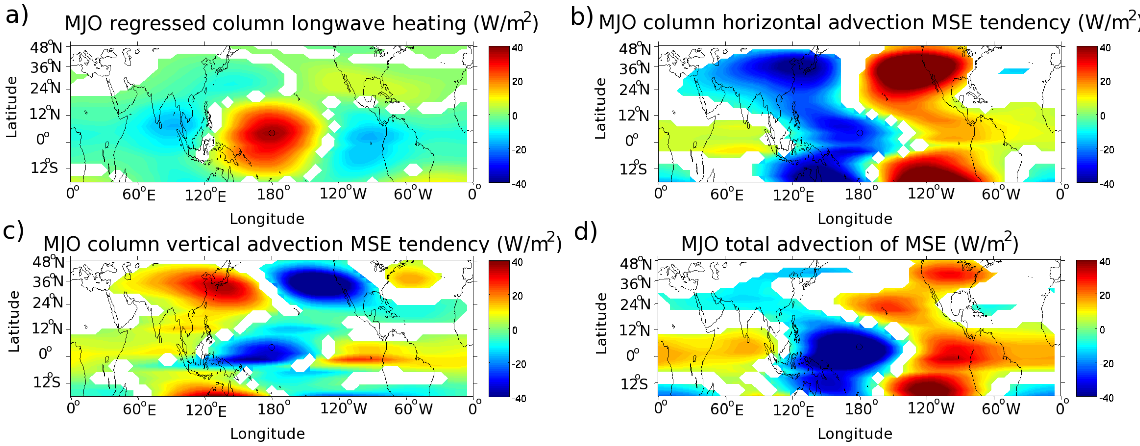

FIG. 8. Leading terms in the MJO regressed column MSE budget. a) Column integrated long wave radiation forcing; b) Column integrated horizontal advection of MSE; c) Column integrated vertical advection of MSE (equivalent to column integrated MSE convergence); d) Total column integrated advection of MSE.

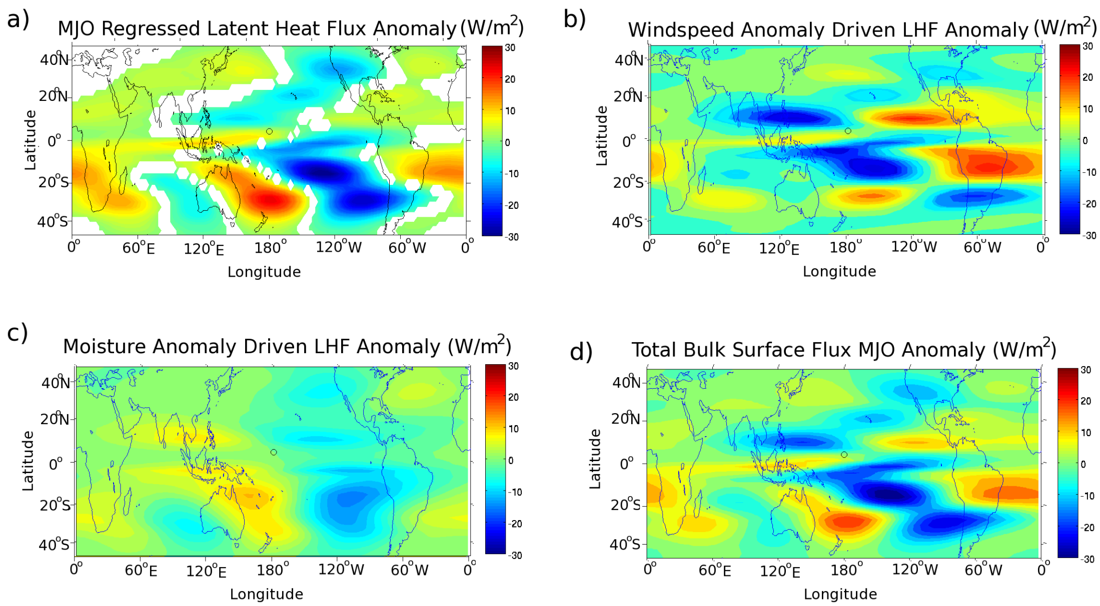

FIG. 9. Latent Heating Terms. a) MJO regressed Latent Heat Flux Anomaly; b) MJO Latent Heating anomaly attributable to changes in surface level windspeed in a bulk surface flux calculation; c) MJO Latent Heating anomaly attributable to changes in surface level moisture content in a bulk surface flux calculation; d) Total bulk surface scheme latent heat flux anomaly.

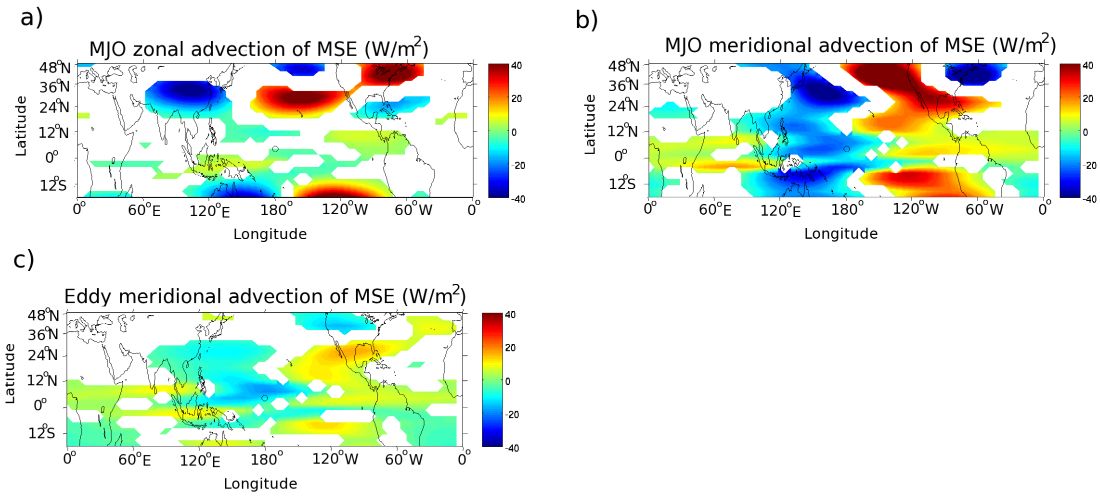

FIG. 10. a) Column integrated zonal advection of MSE; b) Column integrated meridional advection of MSE; c) column integrated, MJO regressed, high frequency v-high frequency h advection.

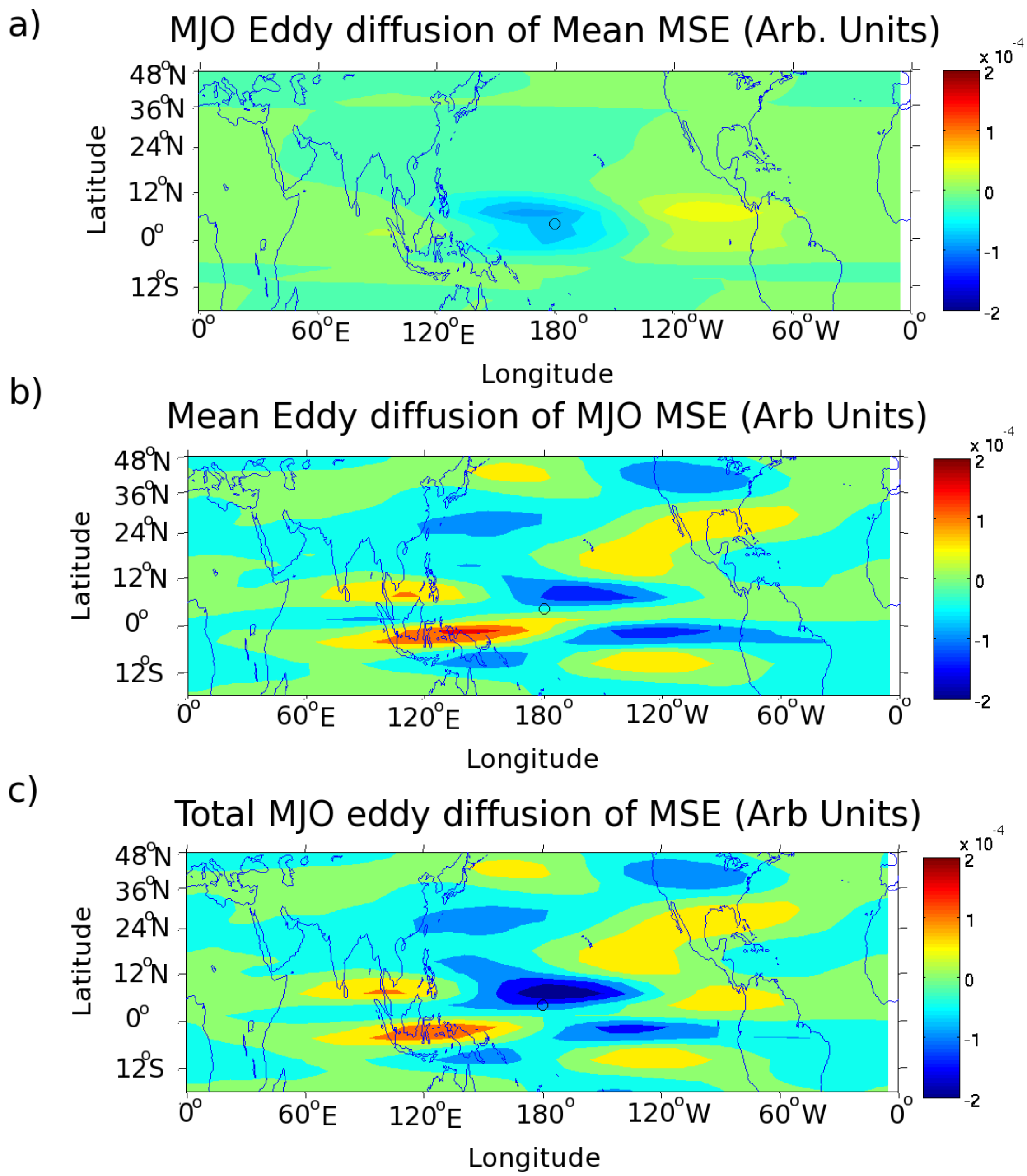

FIG. 11. Eddy Diffusion of MSE anomalies. a) Diffusion of mean MSE by MJO eddy anomalies; b) Diffusion of eddy MSE anomalies by mean eddy activity; c) Total eddy diffusion of MSE. All figures are in arbitrary but consistent units.

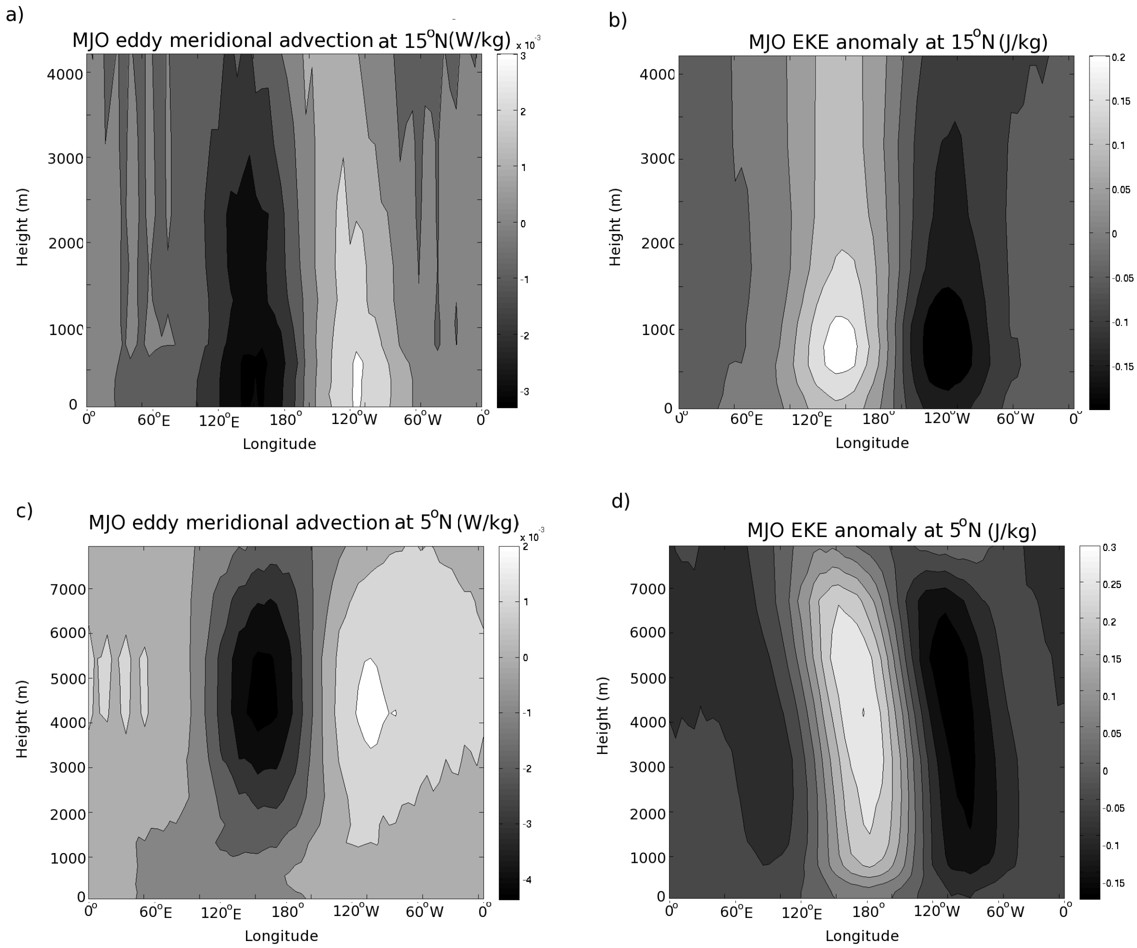

FIG. 12. a) Anomalous Eddy Meridional Advection of MSE at N; b) Eddy Kinetic Energy (EKE) anomaly at N; c) Anomalous Eddy Meridional Advection of MSE at N; and d) Eddy Kinetic Energy (EKE) anomaly at N. MJO regression point is located at Note the differences in vertical scale between the first and second pair of figures.

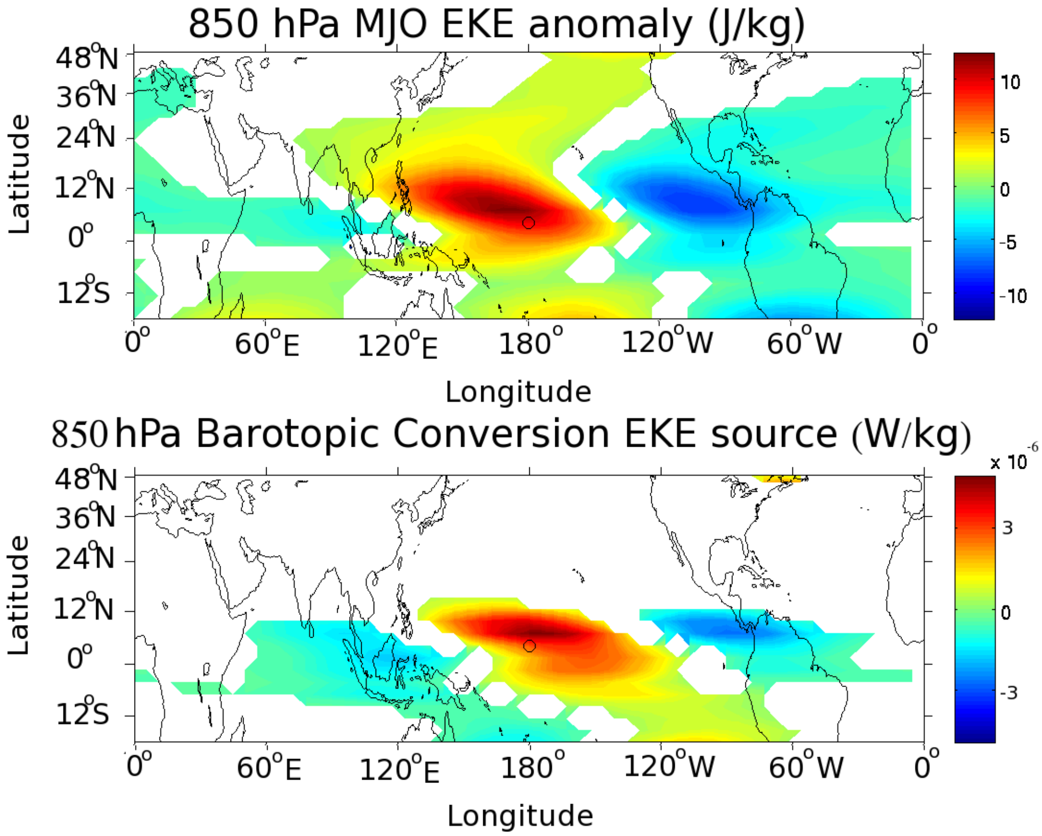

FIG. 13. a) The MJO regressed EKE anomaly at 850 hPa; b) EKE source due to barotropic conversion of energy from the large scale winds at 850 hPa.